

ON THE MODELLING AND IDENTIFICATION  
OF HARMONIC DRIVE SYSTEMS

Hamid D. Taghirad

CIM-TR-97-02

January 29, 1997

Centre for Intelligent Machines  
McGill University  
Montréal, Québec, Canada

Postal Address: 3480 University Street, Montréal, Québec, Canada H3A 2A7  
Telephone: (514) 398-6319    Telex: 05 268510    FAX: (514) 398-7348  
Email: [cim@cim.mcgill.ca](mailto:cim@cim.mcgill.ca)



## ABSTRACT

The unique performance features of harmonic drives, such as high gear ratios and high torque capacities in a compact geometry, justify their widespread industrial application, especially in robotics. However, harmonic drives can exhibit surprisingly more complex dynamic behavior than conventional gear transmissions. In this report, a systematic way to capture and rationalize the dynamic behavior of the harmonic drive systems is examined. Simple and accurate models for compliance, hysteresis, and friction are proposed, and the model parameters are estimated using least-squares approximation for linear and nonlinear regression models. A statistical measure of variation is defined, by which the reliability of the estimated parameter for different operating condition, as well as the accuracy and integrity of the proposed model is quantified. Finally, the model performance is assessed by a simulation verifying the experimental results.

## RÉSUMÉ

Les performances uniques de l'entraînement à harmoniques, telles que rapports d'engrenage élevés ainsi que de fortes capacités de couple, justifient leur applications industrielles très répandues, particulièrement en robotique. Cependant, l'entraînement à harmoniques peut présenter un comportement dynamique plus complexe que les transmissions d'engrenage conventionnelles. Dans cette thèse, nous proposons une étude systématique et rationnelle du comportement dynamique de l'entraînement à harmoniques. Des modèles simples et précis pour l'élasticité, l'hystérésis et le frottement sont proposés, et les paramètres du modèle sont estimés par la méthode des approximations des moindres carrés pour modèles linéaire et non-linéaire regressifs. Nous définissons une mesure statistique de variation avec laquelle on quantifie non seulement la fiabilité des paramètres estimés pour différentes conditions d'opération mais aussi la précision et l'intégrité du modèle proposé. Finalement, les performances du modèle sont illustrées par simulation, vérifiant ainsi les résultats expérimentaux.

## ACKNOWLEDGEMENTS

I wish to extend my sincere gratitude and appreciation to my research advisor, Dr. Pierre R. Bélanger, for his excellent guidance throughout this research. I would like to express my appreciation to A. Helmeý for his involvements in the experiments and my fellow students at the Centre for Intelligent machines for many interesting and enjoyable discussions. In particular, I am grateful to my office-mates Mohammed Seddik Djouadi for his assistance in the French translation of the abstract, and Michael Glaum for proof reading some parts of this report.

## CONTENTS

Abstract . . . . .	1
Résumé . . . . .	1
Acknowledgements . . . . .	2
List of Figures . . . . .	5
List of Tables . . . . .	7
1. Introduction . . . . .	9
1.1. Harmonic Drive Systems . . . . .	9
1.1.1. The Principles of Operation . . . . .	9
1.1.2. Performance Features . . . . .	10
1.2. Experimental Setup . . . . .	11
1.3. Identification Methods . . . . .	12
1.3.1. Linear Regression Models . . . . .	12
1.3.2. Nonlinear Regression Model . . . . .	13
1.3.3. Discrete and Continuous Time Models . . . . .	14
1.3.4. Methods of Signal Differentiation . . . . .	15
2. Modelling and Simulation . . . . .	17
2.1. DC Motor Modelling and Simulation . . . . .	17
2.1.1. Friction Simulation Block . . . . .	18
2.2. Harmonic Drive Modelling and Simulation . . . . .	20
2.2.1. Model 1: Ideal Model . . . . .	22
2.2.2. Model 2: Compliance . . . . .	23
2.2.3. Model 3: Friction and Compliance . . . . .	23
2.3. Overall System Modelling and Simulation . . . . .	25
3. DC-Motor Identification . . . . .	27
3.1. Introduction . . . . .	27
3.2. Linear Regression Model . . . . .	27
3.3. Nonlinear Regression Model . . . . .	28
3.4. Simulation Check . . . . .	30
3.5. Experiments Outline . . . . .	31
3.6. Final Identification Results . . . . .	32
3.7. Simulation and Experiment Comparison . . . . .	33
4. Harmonic Drive Identification . . . . .	39
4.1. Introduction . . . . .	39
4.2. Harmonic Drive Compliance . . . . .	39
4.2.1. Regression Models . . . . .	41
4.2.2. Experimental Results . . . . .	42
4.3. Harmonic Drive Friction . . . . .	50
4.3.1. Regression Models . . . . .	51
4.3.2. Experimental Results . . . . .	52
5. Modelling and Identification Verification . . . . .	59
5.1. System under Locked-Load Motion . . . . .	59
5.2. System under Free-Motion . . . . .	60
5.3. Comparison of the Simulation and Experiment . . . . .	61

5.4. Parameter Sensitivity Study . . . . .	62
6. Conclusions . . . . .	65
References . . . . .	67
Appendix A. Simulation Verification Plots . . . . .	69

## LIST OF FIGURES

1	<i>Harmonic drive components . . . . .</i>	9
2	<i>A picture of the experimental setup for free-load experiments and its schematics</i>	11
3	<i>A picture of the experimental setup for locked load experiment . . . . .</i>	12
4	<i>Black box representation of the DC motor . . . . .</i>	17
5	<i>Saturation of the servo amplifier current . . . . .</i>	17
6	<i>DC motor model simulated on Simulink . . . . .</i>	18
7	<i>A moving mass <math>M</math> under driving and friction forces . . . . .</i>	18
8	<i>The Modified friction curve used in the simulation to avoid chattering velocity</i>	19
9	<i>The simulation result of a moving mass with initial velocity; Discontinuous friction with <math>\epsilon = 10^{-8}</math> . . . . .</i>	20
10	<i>The simulation result of a moving mass with initial velocity; Discontinuous friction with <math>\epsilon = 10^{-4}</math> . . . . .</i>	21
11	<i>The simulation result of a moving mass with initial velocity; Continuous friction . . . . .</i>	21
12	<i>Ideal transmission model of harmonic drive . . . . .</i>	22
13	<i>Block box illustration of harmonic drive . . . . .</i>	22
14	<i>Transmission model of harmonic drive with compliance . . . . .</i>	23
15	<i>Transmission model of harmonic drive with compliance and friction . . . . .</i>	23
16	<i>Harmonic drive model simulated on Simulink . . . . .</i>	25
17	<i>Overall System model simulated on Simulink: Free load case . . . . .</i>	25
18	<i>Overall System model simulated on Simulink: Locked load case . . . . .</i>	26
19	<i>The friction model consists of static and viscous friction . . . . .</i>	28
20	<i>The friction model consists of static, viscous, Stribeck friction . . . . .</i>	29
21	<i>The Simulink DC motor model for testing the identification process . . . . .</i>	30
22	<i>Different current input signals . . . . .</i>	32
23	<i>Typical experimental input-output signals . . . . .</i>	33
24	<i>Comparison of simulation to experiments for low velocity input . . . . .</i>	34
25	<i>Comparison of simulation to experiments for high velocity input . . . . .</i>	35
26	<i>Comparison of simulation using identified parameter and modified identified parameters to experiment for low velocity input . . . . .</i>	36
27	<i>Comparison of simulation using identified parameter and modified identified parameter to experiment for high velocity input . . . . .</i>	36
28	<i>Flexspline measured torsion in locked load experiment, which possess hysteresis</i>	40
29	<i>Modified Dahl model for structural damping and cubic stiffness model compared to an experiment . . . . .</i>	43
30	<i>Structural damping model, comparison of different velocity exponents; solid: experiment, dashed: <math>\alpha = 1</math>, dash-dotted: <math>\alpha = 0.5</math>, and dotted: <math>\alpha = 0.1</math> . . . . .</i>	44

31	<i>Comparison of two models with <math>\alpha = \frac{1}{2}</math> and <math>\alpha = \frac{1}{3}</math> . . . . .</i>	45
32	<i>Comparison of hysteresis curve with optimal <math>\alpha</math> and <math>\alpha = \frac{1}{2}</math> . . . . .</i>	46
33	<i>Comparison of the experimented hysteresis loop with the estimated cubic model of stiffness; solid: experiment, dashed: linear stiffness model, dash-dotted: cubic stiffness model . . . . .</i>	47
34	<i>Comparison of the experimented hysteresis loop with nominal result of linear stiffness model . . . . .</i>	49
35	<i>Comparison of the experimented torque curve with nominal result of linear stiffness model . . . . .</i>	49
36	<i>Transmission model of harmonic drive with compliance and friction . . . . .</i>	50
37	<i>Comparison of the least square estimated torque to experiment for four different inputs; dotted: experiment, solid: estimated . . . . .</i>	52
38	<i>Comparison of nominal model torque to experiments for sinusoid inputs; dotted: experiment, solid: estimated . . . . .</i>	54
39	<i>Comparison of nominal model torque to experiments for other types of inputs; dotted: experiment, solid: estimated . . . . .</i>	54
40	<i>Low velocity experiment: indication of break out in velocity curve . . . . .</i>	55
41	<i>Identified friction curve . . . . .</i>	56
42	<i>Comparison of nominal model torque to experiments for low speed experiments</i>	57
43	<i>System under locked-load motion simulated on Simulink for model verification purpose. Top: System; Mid: DC-motor; Bot: Harmonic drive . . . . .</i>	59
44	<i>System under free motion simulated on Simulink for model verification purpose. Top: System; Mid: DC-motor; Bot: Harmonic drive . . . . .</i>	60
45	<i>Simulation verification for system under free and locked-load motion; Solid : Experiment, Dotted : Simulation . . . . .</i>	61
46	<i>Comparison of the experiment with the complete and simplified model, where the significance of Coulomb and viscous friction are examined separately; Solid : Experiment, Dash-dotted : Complete model, Dashed : Simplified model . . . . .</i>	62
47	<i>Comparison of the experiment with the complete and simplified model, where the significance of stiffness and structural damping are examined separately; Solid : Experiment, Dash-dotted : Complete model, Dashed : Simplified model . . . . .</i>	63
48	<i>Locked-load simulation verification: Sinusoid input, 80% of maximum amplitude.</i>	69
49	<i>Locked-load simulation verification: Asymmetric sinusoid input, with maximum amplitude. . . . .</i>	70
50	<i>Locked-load simulation verification: Asymmetric sinusoid input, 50% of maximum amplitude. . . . .</i>	70
51	<i>Locked-load simulation verification: Sinusoid input, 50% of maximum amplitude.</i>	71



52 Locked-load simulation verification: Inverted sinusoid input, 50% of maximum amplitude. . . . .	71
53 Locked-load simulation verification: Trianglur input, 50% of maximum amplitude. . . . .	72
54 Locked-load simulation verification: Composite Sine input, 50% of maximum amplitude. . . . .	72
55 Free-motion simulation verification: 1.2 Hz sinusoid input . . . . .	73
56 Free-motion simulation verification: 1.4 Hz sinusoid input . . . . .	73
57 Free-motion simulation verification: 1.6 Hz sinusoid input . . . . .	74
58 Free-motion simulation verification: 1.8 Hz sinusoid input . . . . .	74
59 Free-motion simulation verification: 2 Hz sinusoid input . . . . .	75
60 Free-motion simulation verification: 2.5 Hz sinusoid input . . . . .	75

## LIST OF TABLES

1 <i>Nominal DC motor parameter used in simulation, compared to the linear and nonlinear regression results . . . . .</i>	30
2 <i>Least square results of linear regression model for the DC motor . . . . .</i>	32
3 <i>Least-square results of modified linear regression model for the DC motor . . . . .</i>	37
4 <i>Least square results of linear regression model of the harmonic drive for two velocity exponents <math>\alpha = \frac{1}{2}</math> and <math>\alpha = \frac{1}{3}</math> . . . . .</i>	45
5 <i>Least square results of non linear regression model of harmonic drive compliance . . . . .</i>	46
6 <i>Least square results of linear regression model of harmonic drive compliance with cubic stiffness . . . . .</i>	48
7 <i>Least square results of linear regression model for high speed friction terms . . . . .</i>	53
8 <i>Least square results of Stribeck friction coefficients in harmonic drive . . . . .</i>	56

.

## 1. INTRODUCTION

In this report we present a methodology to model, simulate and identify the model parameters of the harmonic drive systems. The report is divided into six sections. In this section after introducing the harmonic drive system, the identification models, their properties, and the mathematical methods needed to solve the identification problem is discussed. Section 2 is devoted to the the modelling of the DC-motor, the harmonic drive and the overall system for free load and locked load, giving the simulation routines built in Simulink for each part. Section 3 introduces the identification of the DC-motor. In this section different regression models for the system is presented and the final identified parameter of the system and simulation verification is given. In Section 4 the identification methods for the harmonic drive is presented. Finally, in Section 5 the modelling and identification scheme is validated by experiments, and the significance of the nonlinear model is assessed by simulations through a parameter sensitivity study.

### 1.1. Harmonic Drive Systems.

#### 1.1.1. *The Principles of Operation.*

Developed in 1955 primarily for aerospace applications, harmonic drives are high-ratio and compact torque transmission systems. Every harmonic drive consists of the three components illustrated in Figure 1. The wave generator is a ball bearing assembly with a rigid, elliptical inner race and a flexible outer race. The flexspline is a thin-walled, flexible cup adorned with small, external gear teeth around its rim. The circular spline is a rigid ring with internal teeth machined along a slightly larger pitch diameter than those of the flexspline. When assembled, the wave generator is nested inside the flexspline, causing the flexible circumference to adopt the elliptical profile of the wave generator, and the external teeth of the flexspline to mesh with the internal teeth on the circular spline along the major axis of the wave generator ellipse.

If properly assembled, all three components of the transmission can rotate at different but coupled velocities on the same axis. To use the harmonic drive for speed

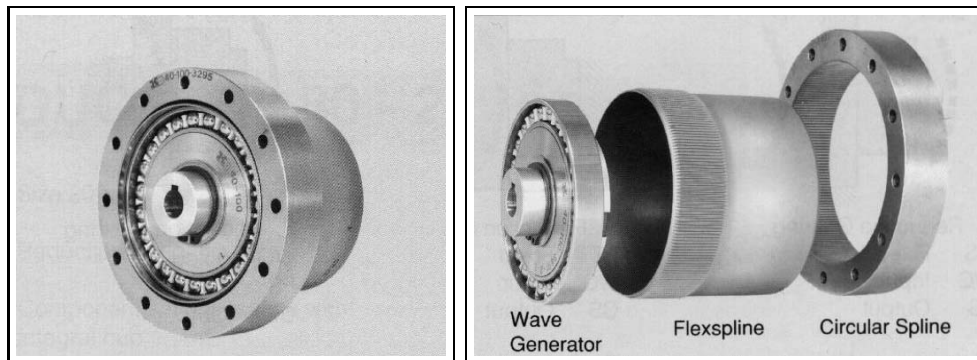


FIGURE 1. *Harmonic drive components*

reduction, the wave generator is mounted on the electric motor shaft, and the output is conveyed either through the flexspline while the circular spline is fixed or through the flexspline while the circular spline is fixed. In the latter case, by rotation of the wave generator the zone of gear-tooth engagement is carried with the wave generator major elliptical axis. When this engagement zone is propagated  $360^\circ$  around the circumference of the circular spline, the flexspline which contains fewer teeth than the circular spline, will lag by that fewer number of teeth relative to the circular spline. Through this gradual and continuous engagement of slightly offset teeth, every rotation of the wave generator moves the flexspline a small angle back on the circular spline, and through this unconventional mechanism, gear ratios up to 320 : 1 can be achieved in a single transmission.

Since the harmonic drive has three rotational ports, by using different combinations of rotations on these ports, numerous differential-gearing functions and reduction ratios can be achieved. In most popular configuration, the circular spline is fixed to ground and a low-torque, high-speed motor driving the wave generator can produce high-torque, low-speed rotation on the flexspline.

#### 1.1.2. *Performance Features.*

Typical gear ratios of commercial drives range from 50:1 to 320:1, and efficiencies can approach 90 %. the smallest transmission can provide respectable maximum torque output of about 3.5 N-m, while the heavy-duty units boast up to 10,000 N-m of torque capacity.

Because of its unique performance features, the harmonic drive displays performance features both superior and inferior to conventional gear transmissions. These advantages and disadvantages are itemized as follows:

- Performance advantages:
  - : High torque capacity:  
Since torque is transmitted through multiple-tooth contact, harmonic drive can withstand high torque at small pitch diameters.
  - : Concentric geometry:  
Since all three harmonic drive components are concentric and coaxial, designer can drastically reduce power-train size and complexity.
  - : Lightweight and compact:  
Requiring only three basic elements, the harmonic drive can deliver extremely high gear ratios in small package.
  - : Zero backlash:  
Natural gear preloading and predominantly radial tooth engagement eliminate virtually all transmission backlash.
  - : High efficiency:  
If properly lubricated, typical efficiencies of harmonic drive transmission can reach 80 to 90 percent (different claims about this exist).
  - : Back drivability:  
Due to their high efficiency, wave generator rotation can be driven through the flexspline or circular spline.
- Performance disadvantages:

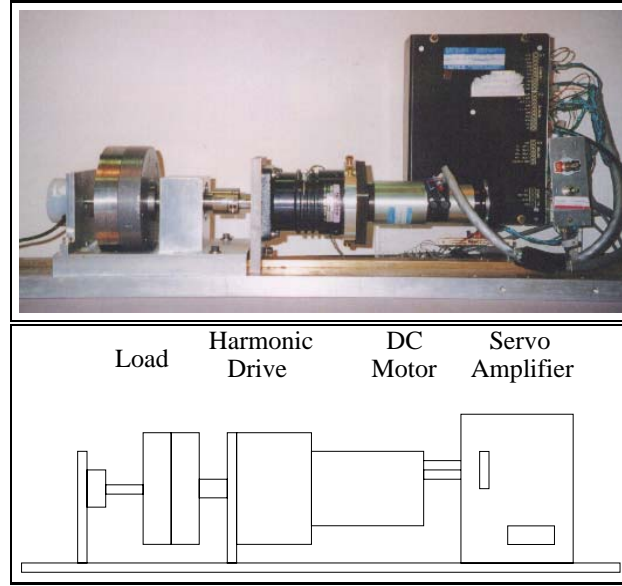


FIGURE 2. *A picture of the experimental setup for free-load experiments and its schematics*

◦: High flexibility:

Due to the high load seen by the wave generator and gear teeth, moderate operating torques can produce substantial transmission torsion.

◦: Resonance vibration:

Since torque fluctuations produced by kinematic error can interact with the low stiffness of the transmission to excite resonances, high vibration amplitudes may be generated in some operating ranges.

◦: Nonlinearity:

Both flexibility and frictional losses in the drive exhibit highly nonlinear behaviour.

◦: Low insight knowledge:

Compared to the conventional gear transmissions, relatively little exploration has been done of the unusual operating mechanisms in the harmonic drive.

The unique performance features of the harmonic drive have captured the attention of designers in many fields. It has been used in industrial robots, assembly equipment, and measuring instruments, as well as heavy duty applications such as machine tools and printing presses. Additionally, space and aircraft systems often employ harmonic drives for their light weight and compact geometry.

## 1.2. Experimental Setup.

A harmonic drive testing station is employed to monitor the behaviour of the system in free-load and locked-load experiments. A picture of the setup and its schematics are illustrated in Figures 2 and 3, in which the harmonic drive is driven by a DC motor, and a load inertia is used to simulate the robot arm for free motion.

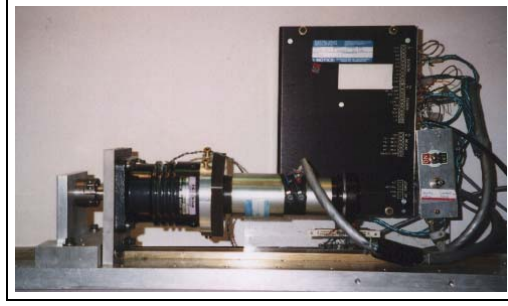


FIGURE 3. A picture of the experimental setup for locked load experiment

Also a positive locking system is designed such that the output load can be locked to the ground for loacked-load experiments. In this setup, a brushed DC motor from Electro-Craft is used. Its weight is 1360 grammes, with maximum rated torque of  $0.15 \text{ Nm}$ , and torque constant of  $0.0543 \text{ Nm/amp}$ . The servo amplifier is a 40 Watts Electro-Craft power amplifier. The harmonic drive is from RHS series of HD systems, with gear ratio of 100:1, and rated torque of  $40 \text{ Nm}$ .

The setup is equipped with a tachometer to measure the motor velocity, and an encoder on the load side to measure the output position. The current applied to the DC motor is measured from the servo amplifier output and the output torque is measured by a Wheatstone bridge of strain gauges mounted directly on the flexspline [14]. These signals were processed by several data acquisition boards and monitored by a C-30 Challenger processor executing compiled computer C codes.

### 1.3. Identification Methods.

#### 1.3.1. Linear Regression Models.

There are two general method for identification introduced in the literature. In the first method a parametrized mathematical model of the system is assumed, where the parameters of the model are subject to identification. The second method challenges more complex systems, where a parametrized mathematical model is not available. In this case usually a linear model with a specific order may assumed to capture the behavior of the system, where the parameters of the model is subject to identification. In this study we use the first case in which we assume that the mathematical model of the system can be derived from physical principles.

A set of experimental input-output data is used for identification of the model parameters. Given the set of input-output pairs  $\{u_i, y_i\}_{i=1}^m$  for each pair the input-output relation can be generally written as  $m$  equation in the form:

$$\mathbf{f}(y_i, u_i, \boldsymbol{\theta}) = \mathbf{0} \quad ; \quad \text{for } i = 1, 2, \dots, m \quad (1)$$

where the unknown model parameters are collected in the rows of the vector  $\boldsymbol{\theta}$ . Equation 1 implies that the input-output relation for the system depends only on the input and output signals and the identification parameters. This is not generally true, since some information, such as the derivatives of the input-output signals, may intervene with the input-output relation.

Suppose Equation 1 is linear in  $\theta$  then it can be written in the form of:

$$\mathbf{A}\theta = \mathbf{b} \quad (2)$$

where  $\mathbf{A}$  is an  $m \times n$  matrix,  $\theta$  is the  $n \times 1$  column vector of identification parameters,  $\mathbf{b}$  is the  $m \times 1$  column vector, and  $m > n$ . If the model is perfect, i.e. the input output signals are noise free, and the mapping  $\mathbf{A}$  is of full rank, then this system of overdetermined equations has a unique solution which are the exact identification parameters. However, these condition is not satisfied in practice and there is no exact solution to the system expressed in Equation 2. If the mapping is of full rank, then a unique approximate solution can be found, which verifies Equation 2 with the minimum Euclidean error. This solution is called the *least-square* solution and can be expressed by *Moore–Penrose generalized inverse* of the rectangular matrix  $\mathbf{A}$ ,

$$\theta_l = \mathbf{A}^I \mathbf{b} \quad (3)$$

where

$$\mathbf{A}^I := (\mathbf{A}^T \mathbf{A})^{-1} \mathbf{A}^T \quad (4)$$

Direct calculation of  $\mathbf{A}^I$  can be numerically intractable due to ill conditioning. Several other numerical techniques, such as orthogonal decomposition, Householder reflections, or Cholesky factorization can be used to avoid ill conditioning. These methods are well developed, and most efficient packages such as Matlab incorporate them. [12]

### 1.3.2. Nonlinear Regression Model.

Consider the general input–output relation given in Equation 1. If this relation is not linear in  $\theta$  then the model is called nonlinear regression. repeating Equation 1 in terms of unknown parameters  $\theta$  only:

$$\mathbf{f}(\theta) = \mathbf{0} \quad (5)$$

$\mathbf{f}$  is an  $m \times 1$  vector valued function nonlinear in  $\theta$ . A solution in this case may or may not exist, and if it exists it may be nonunique. The main idea in identification, however, is to find an approximate solution  $\theta_l$  which minimizes the norm of error:

$$e(\theta) = \frac{1}{2} \mathbf{f}^T \mathbf{f} \quad (6)$$

A solution can be computed iteratively, using *Newton–Gauss* method. First, an initial guess of  $\theta$ , say  $\theta^0$ , is given, then a sequence of  $\theta^k$  is generated, where

$$\theta^{k+1} = \theta^k + \Delta \theta^k \quad (7)$$

and the least-square solution of the system is,

$$\Delta \theta^k = -(\mathbf{J}^T \mathbf{J})^{-1} \mathbf{J}^T \mathbf{f}(\theta^k) \quad (8)$$

where  $\mathbf{J}(\theta)$  defined as the  $m \times n$  Jacobian matrix of the vector function  $\mathbf{f}(\theta)$ , i.e.,

$$\mathbf{J}(\theta) = \frac{\partial \mathbf{f}(\theta)}{\partial \theta} \quad (9)$$

This iteration should be proceed until  $\|\Delta \theta\| < \epsilon$ . Calculation of the inverse in Equation 8 can be numerically intractable due to ill conditioning. Therefore, other

numerical approaches such as orthogonal decomposition, Householder reflection, or Cholesky decomposition might be numerically more stable.

### 1.3.3. Discrete and Continuous Time Models.

Two class of models can be considered for identification process, discrete and continuous time models. For a time invariant system the discrete time model can be represented by a difference equation or a z-domain transfer function. For instance a finite impulse response (FIR) filter can be represented as:

$$y_k = b_1 u_{k-1} + b_2 u_{k-2} + \cdots + b_m u_{k-m} \quad (10)$$

or

$$y(z) = (b_1 z^{-1} + b_2 z^{-2} + \cdots + b_m z^{-m})u(z) \quad (11)$$

while an infinite impulse response (IIR) filter is represented by the following difference equation:

$$y_k = b_1 u_{k-1} + b_2 u_{k-2} + \cdots + b_m u_{k-m} - a_1 y_{k-1} - a_2 y_{k-2} - \cdots - a_n y_{k-n} \quad (12)$$

or

$$\frac{y(z)}{u(z)} = \frac{b_1 z^{-1} + b_2 z^{-2} + \cdots + b_m z^{-m}}{1 + a_1 z^{-1} + a_2 z^{-2} + \cdots + a_n z^{-n}} \quad (13)$$

On the other hand, to model an analog filter in the continuous time domain a differential equation is required, i.e.,

$$\frac{d^n y}{dt^n} + a_1 \frac{d^{n-1} y}{dt^{n-1}} + \cdots + a_n y = b_1 \frac{d^{m-1} u}{dt^{m-1}} + \cdots + b_m u \quad (14)$$

In our experimental setup the input-output signals are available as a discrete sequence in time, and the derivatives of the signals are not available. Therefore, the discrete time models more directly transformed into the linear regression model. Consider Equation 12 to be rewritten in the form,

$$y_k = \phi_k^T \boldsymbol{\theta} \quad (15)$$

where

$$\phi_k^T = [-y_{k-1}, -y_{k-2}, \dots, -y_{k-n}, u_{k-1}, u_{k-2}, \dots, u_{k-m}] \quad (16)$$

Equation 15 can be directly transformed into linear regression model of

$$\mathbf{A} \boldsymbol{\theta} = \mathbf{b} \quad (17)$$

where,

$$\mathbf{A} = \begin{bmatrix} \phi_k^T \\ \phi_{k-1}^T \\ \vdots \\ \phi_1^T \end{bmatrix} ; \quad \mathbf{b} = \begin{bmatrix} y_k \\ y_{k-1} \\ \vdots \\ y_1 \end{bmatrix} \quad (18)$$

$$\boldsymbol{\theta}^T = [a_1, a_2, \dots, a_n, b_1, b_2, \dots, b_m] \quad (19)$$

However, this transformation is not directly feasible for the continuous time domain models (Equation 14), since the derivatives of the signals are not available. A naive



way to overcome this problem is to differentiate the signals numerically. This is not an appropriate method in presence of noise, for it will magnify the effect of noise. There are better methods to overcome this problem which will be discussed next.

#### 1.3.4. Methods of Signal Differentiation.

A first method to represent the continuous time model as regression model is discretization. There are different method of discretization including backward difference, bilinear transformation (with or without frequency warping), impulse invariant transformation, and zero-pole matched transformation. For instance in the bilinear transformation we replace  $s$  (Laplace variable) with  $z$  by the following relation, where  $T_s$  is the sampling time.

$$s = \frac{2}{T_s} \frac{1 - z^{-1}}{1 + z^{-1}} \quad (20)$$

All of these methods have two main problems. Firstly there is no filtering on their structure; therefore, noise magnification will appear on the results in some extent. Secondly, they are designed to transform linear continuous models into discrete ones. Thus, for nonlinear models, the transformation is complicated and practically infeasible.

A second method is analog filtering and then discretization. To describe the method let us consider the following second-order system, i.e.,

$$\begin{aligned} M\ddot{y} + B\dot{y} + Ky &= u \\ (Ms^2 + Bs + K)y &= u \end{aligned} \quad (21)$$

First multiply both sides by a low pass analog filter. The filter can be any type, but at least second order. Two natural candidate filters are:

$$H_1(s) = \frac{\omega_0^2}{s^2 + \sqrt{2}\omega_0 s + \omega_0^2} \quad \text{or} \quad H_2(s) = \frac{\omega_0^2}{(s + \omega_0)^2} \quad (22)$$

Multiplying Equation 21 with  $H_2$  gives after some manipulation,

$$(M\omega_0^2)y + (B - 2M\omega_0)y_{fd} + (K - M\omega_0^2)y_f = u_f \quad (23)$$

where

$$y_{fd} = \frac{s\omega_0^2}{(s + \omega_0)^2}y, \quad y_f = \frac{\omega_0^2}{(s + \omega_0)^2}y, \quad u_f = \frac{\omega_0^2}{(s + \omega_0)^2}u \quad (24)$$

which represents the derivative of filtered signal and the filtered signals respectively.

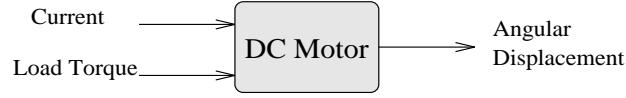
In practice since  $y$  and  $u$  are given in discrete time domain, in order to find the filtered signals, we have to transform the filter also into discrete time domain. This can be done again with any method of discretization. Still this method is not applicable for nonlinear systems, although the noise magnification is recovered.

A third method is a modification of the second method in the discrete time domain. In this method we design first a digital filter to clean the measured signal from noise and then use numerical differentiation to obtain the derivatives. This method is also feasible for nonlinear systems. There is always, however, a phase distortion in the

signal. To avoid this problem, in our identification process the experimental signals are filtered using a fifth order Butterworth filter, by zero-phase distortion routine <sup>1</sup>.

---

<sup>1</sup>Function *filtfilt* in Matlab

FIGURE 4. *Black box representation of the DC motor*

## 2. MODELLING AND SIMULATION

### 2.1. DC Motor Modelling and Simulation.

DC motor can be viewed as a black box with two input, input current, and load torque, and an output angular displacement (or velocity) as illustrated in Figure 4. The mathematical model for the DC motor can be written as

$$\tau_m = \tau_i + \tau_f + \tau_o \quad (25)$$

where  $\tau_m$  is the motor torque generated by the amplifier current,  $\tau_i$  is the inertial torque,  $\tau_f$  is the friction torque, and  $\tau_o$  is the output torque. It can be shown that,

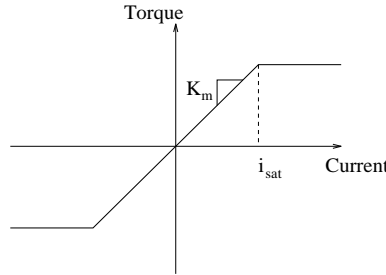
$$\tau_m = K_m \text{sat}(i, i_{\text{sat}}) \quad ; \quad \tau_i = J_m \ddot{\theta} \quad (26)$$

where  $\tau_m$  is bounded due to the current saturation limit of the servo amplifier as illustrated in Figure 5. The friction torque can be expressed by different models such as static and viscous, velocity direction dependent static and viscous, or slip-stick plus static and viscous friction as follows:

$$\tau_f = \begin{cases} T_{v_m} \dot{\theta} + T_{s_m} \text{sign}(\dot{\theta}) \\ T_{v_n} \dot{\theta} u_{-1}(-\dot{\theta}) + T_{v_p} \dot{\theta} u_{-1}(\dot{\theta}) + T_{s_n} \text{sign}(\dot{\theta}) u_{-1}(-\dot{\theta}) + T_{s_p} \text{sign}(\dot{\theta}) u_{-1}(\dot{\theta}) \\ T_{v_m} \dot{\theta} + T_{s_m} \text{sign}(\dot{\theta}) + T_{ss1} \text{sign}(\dot{\theta}) e^{-\left(\frac{\dot{\theta}}{T_{ss2}}\right)^2} \\ T_{v_m} \dot{\theta} + T_{s_m} \text{sign}(\dot{\theta}) + T_{ss1} \frac{\text{sign}(\dot{\theta})}{1 + \left(\frac{\dot{\theta}}{T_{ss2}}\right)^2} \end{cases} \quad (27)$$

where  $u_{-1}(x)$  is the unit step function defined as,

$$u_{-1}(x) = \begin{cases} 1 & \text{if } x > 0 \\ 0 & \text{if } x \leq 0 \end{cases} \quad (28)$$

FIGURE 5. *Saturation of the servo amplifier current*

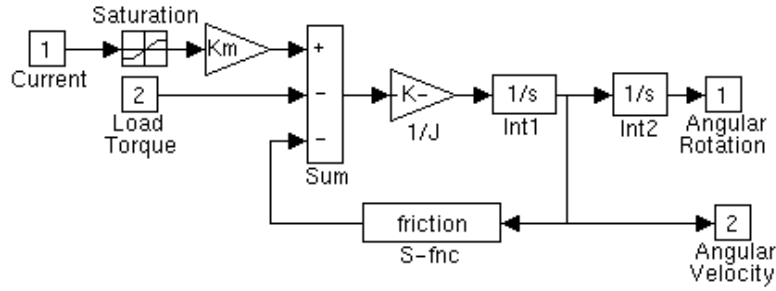


FIGURE 6. DC motor model simulated on Simulink

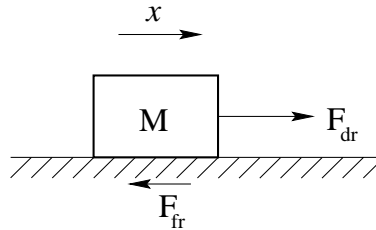
Finally, the equation of motion of the DC motor can be written as:

$$\ddot{\theta} = \frac{1}{J_M}(K_m i - \tau_o - \tau_f) \quad (29)$$

Figure 6 illustrates the block diagram representation of the DC motor model used in the simulation. The model is a simple double integrator, which can incorporate different models of friction. The first input to the system is current,  $i$ , which is limited through the saturation box. The second input is the applied load torque, and the outputs are angular position and velocity.

#### 2.1.1. Friction Simulation Block.

Simulating the friction proves to be a very complicated but important task. In this section we intend to elaborate the technical details of friction simulation in some steps. Consider a simple block with mass  $M$  moving on a rough surface as shown in Figure 7. Suppose the mass is in rest and we start to apply a statically increasing force  $F_{dr}$ . The mass  $M$  will remain stationary until the driving force reaches the static friction. In this region the friction force  $F_{fr} = F_{dr}$ . While increasing the driving force after this limit, the friction force don't depend on the driving force anymore and is a function of the speed, where different models explained in Equation 27 will give the amount of friction force. To simulate this characteristics, a friction block requires two inputs, namely velocity and driving force. This is considered as the first friction block used in the simulation. However, there is a numerical difficulty to implement this idea. Two condition should met to have  $F_{fr} = F_{dr}$ , first the velocity of the mass should be zero, second the driving force is less or equal to the static friction. To implement the first condition, absolute zero velocity can not be used because of

FIGURE 7. A moving mass  $M$  under driving and friction forces

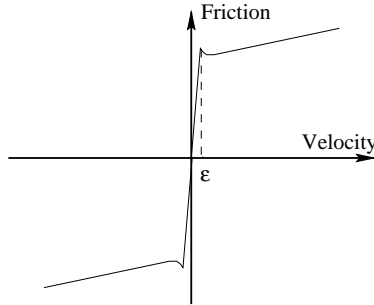


FIGURE 8. *The Modified friction curve used in the simulation to avoid chattering velocity*

the sensitivity of numerical results to round off errors, and a very small threshold  $\epsilon$  should be used. There is a trade off between the numerical sensitivity of the system and the maximum norm of error in finding the optimum value of  $\epsilon$ . To elaborate on that consider the mass  $M$  has an initial velocity, and under no driving force. In practice the mass velocity should slow down until it reaches zero velocity. Figure 9 illustrates this case where  $\epsilon = 10^{-8}$ . For this case since the threshold is too small there is an unrealistic chattering around zero velocity. This may cause a large error for compliant system, and therefore, should be eliminated. Using a larger threshold,  $\epsilon = 10^{-4}$ , reduces the chattering as illustrated in Figure 10, but the final velocity will not decrease to zero but will be bounded by the amount of  $\epsilon$ . The reason for this chattering problem is that in our simulation algorithm, we specify a minimum integration time. Although the routine is using a variable integration step, since there is a lower bound on the integration time the discontinuity generally occurs inside integration subintervals. This cause the velocity and hence the friction force jump between a positive and negative value.

To avoid this problem researchers propose an alternative method for friction simulation [3, 5, 13], which is used in the new version of this block. In this approach the discontinuity is replaced by a curve of finite slope (Figure 8). This model eliminates the need to search for the switching point within an integration subinterval. However, if the slope is large, then small integration step sizes is needed, and hence, the simulation is slow. Also the friction force will not be dependent to the driving force.

In this model the value of bandwidth  $\epsilon$  is dynamically determined due to the characteristics of the system, and the integration step size to ensure avoiding any kind of chattering. The concept behind finding the size of bandwidth is that in the cases where chattering occurs, the bandwidth is large enough that two consequent friction forces are either positive or negative. To find the minimum bandwidth size  $\epsilon$  which provides this condition, let us write the equation of motion for our simple example illustrated in Figure 7. In case where no driving force applied to the mass, (or when the system is at low speed region and we can assume that the friction force is larger than the driving force) we have

$$M\ddot{x} = F_{fr} \quad (30)$$

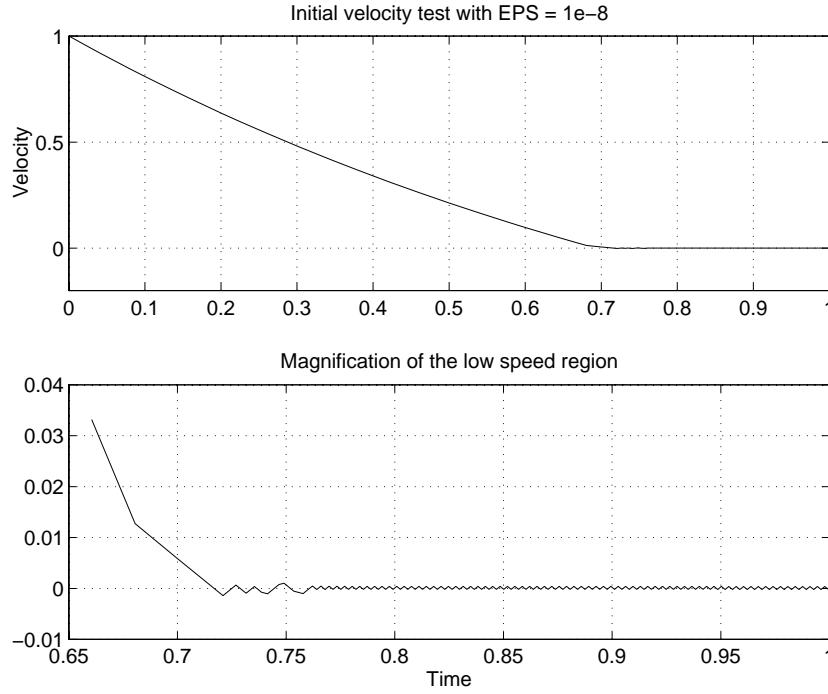


FIGURE 9. The simulation result of a moving mass with initial velocity; Discontinuous friction with  $\epsilon = 10^{-8}$

thus the maximum speed can be approximated by

$$\ddot{x}_{max} = \frac{F_s}{M} \longrightarrow \Delta \dot{x}_{max} = \frac{F_s}{M} \Delta T_{max} \quad (31)$$

where  $F_s$  is the static friction (maximum force), and  $T$  denotes the integration time step. Now to ensure that the next friction point is within the boundary layer, it is sufficient to have at least a boundary layer width equal to:

$$\epsilon = \frac{F_s}{M} \Delta T_{max} \quad (32)$$

Therefore to adjust this boundary layer we require to know the maximum integration time step and the mass or inertia of the system. This algorithm is used to find the variable boundary layer width in the simulation. Figure 11 illustrates the previous example result using this smoothing technique, in which the method is generalized to incorporate the velocity direction dependent friction coefficients.

Although this modification help us to get rid of unrealistic chattering problem, it is important to note that, this model of friction gives unrealistic friction forces within the boundary layer.

## 2.2. Harmonic Drive Modelling and Simulation.

The goal of modelling of the harmonic drive is to discover the simplest representation which can replicate system performance to the desired level of accuracy. This

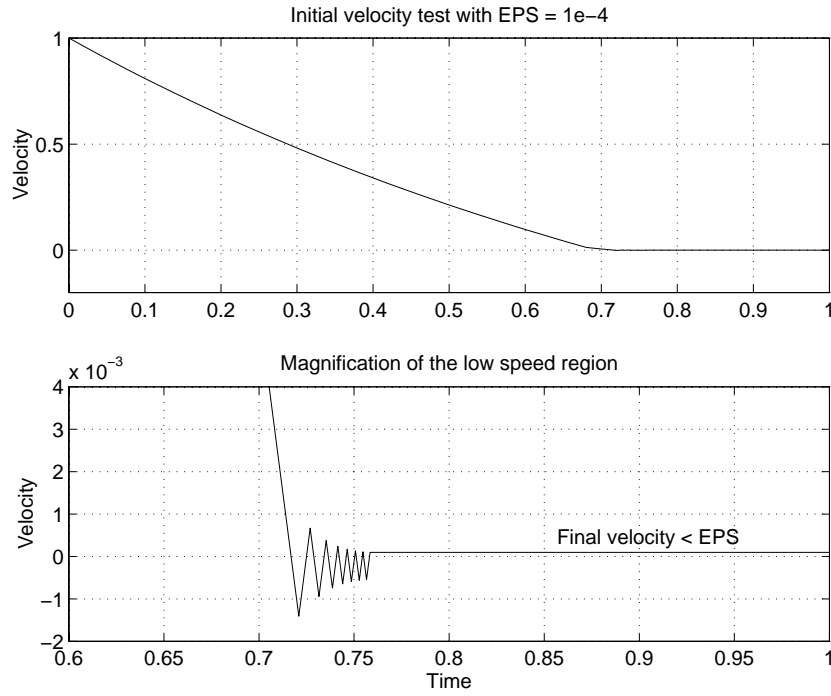


FIGURE 10. The simulation result of a moving mass with initial velocity; Discontinuous friction with  $\epsilon = 10^{-4}$

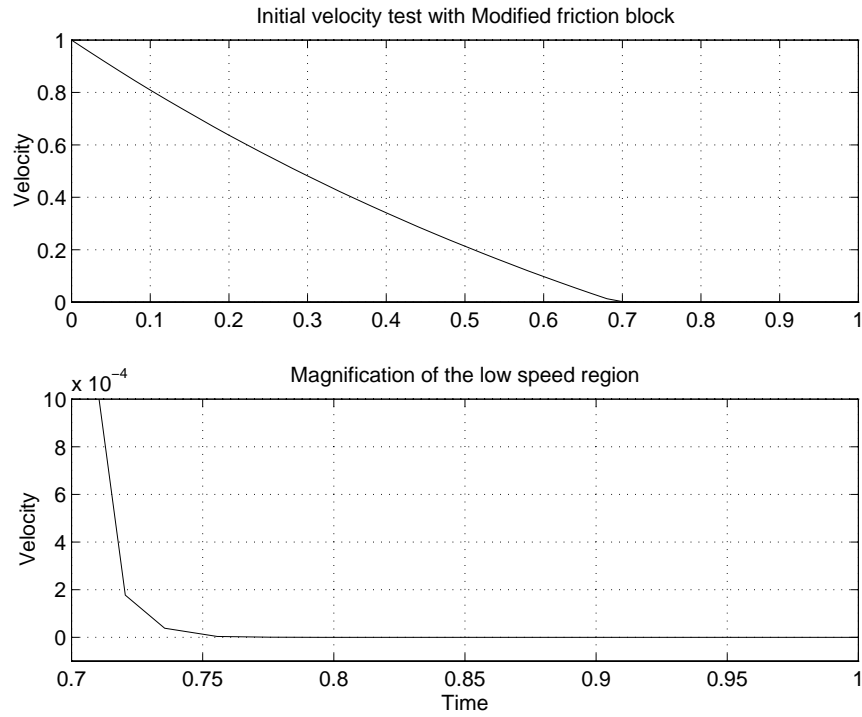


FIGURE 11. The simulation result of a moving mass with initial velocity; Continuous friction

computer model will be the basis for discovering and examining the proposed control algorithms. In this section different models of harmonic drive is presented. The models will come from simple and unrealistic to more complete and realistic ones. It is better to follow the different subsection in order, for better understanding of the final model.

### 2.2.1. Model 1: Ideal Model.

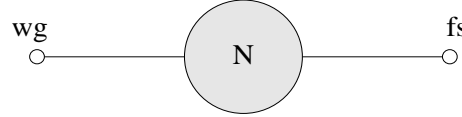


FIGURE 12. *Ideal transmission model of harmonic drive*

Since harmonic drive is a three port transmission unit, two ways of implementing this device is possible in the applications. In this report we only consider one of them which is used in our test setup. In this model circular spline is fixed, wave generator is driven by the input motor, and the output is conveyed through the flexspline. Notice that the direction of rotation in the output shaft is in the opposite direction of that in the input shaft. Considering this fact we made the convention that output rotation is positive if it is in the opposite direction of a positive input rotation to get rid of a minus sign in the equations.

The simplest model for harmonic drive, where no nonlinear source is taken into account, can be named as ideal transmission. This model should be able to describe the gear reduction properties of transmission, which is represent by the following equations.

$$\theta_{wg} = N \theta_{fs} \quad (33)$$

$$\omega_{wg} = N \omega_{fs} \quad (34)$$

$$T_{wg} = \frac{1}{N} T_{fs} \quad (35)$$

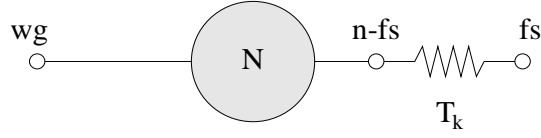
where the notation are defined in Figure 12. Note that the direction of rotation will change if the flexspline node is taken as the output.

Harmonic drive is a two-input two-output system in which inputs and outputs are angular displacement (or velocity), and torque. The input signals to the harmonic drive are wave generator angular position (or velocity), and flexspline torque as shown in Figure 13. This surprising indication can be rationalized by the nature of the system. Clearly the input to the system is the motor rotation which is transmitted through the wave generator by a reduction mechanism to the flexspline. However



FIGURE 13. *Block box illustration of harmonic drive*



FIGURE 14. *Transmission model of harmonic drive with compliance*

the amount of torque transmitted through the system is governed by the amount of torque applied on the flexspline. Suppose there is no output torque and no friction and losses, then the input torque is necessarily zero. That is the reason why the flexspline torque is actually an input signal to the system, and that is true not only for the harmonic drive but also for any other kind of gear transmission.

### 2.2.2. Model 2: Compliance.

To have more realistic model consider now the compliance of the flexspline. Figure 14 illustrates this configuration, where a nonlinear cubic spring is added to the flexspline node [27]. The governing equation of motion can be written as:

$$\begin{cases} \theta_{n_{fs}} = \frac{1}{N}\theta_{wg} \\ T_{wg} = \frac{1}{N}T_{n_{fs}} \end{cases} \quad (36)$$

$$T_k = T_{fs} = T_{n_{fs}} = K_1(\theta_{n_{fs}} - \theta_{fs}) + K_2(\theta_{n_{fs}} - \theta_{fs})^3 \quad (37)$$

Note that other forms for the flexspline compliance can be used here. Finally, solving Equation 37 for  $\theta_{fs}$ ,

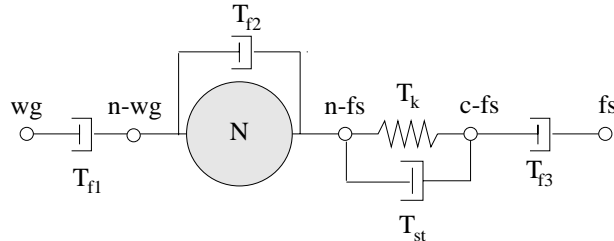
$$\begin{cases} T_{wg} = \frac{1}{N}T_{fs} \\ \theta_{fs} = \frac{1}{N}\theta_{wg} + a^{\frac{1}{3}} - \frac{K_1}{K_2 a^{\frac{2}{3}}} \end{cases} \quad (38)$$

where

$$a = -\frac{T_{fs}}{2K_2} + \frac{1}{18}\sqrt{\frac{3}{K_2^3}} \cdot (4K_1^3 + 27T_{fs}^2 K_2)^{\frac{1}{2}} \quad (39)$$

Equation 38 is an algebraic equation relating input and output signals of the harmonic drive and it is easy to simulate.

### 2.2.3. Model 3: Friction and Compliance.

FIGURE 15. *Transmission model of harmonic drive with compliance and friction*

The bulk of energy dissipation in harmonic drives can be blamed on friction due to gear-tooth meshing action between flexspline and circular spline. Base on this assumption a new model of harmonic drive is shown in Figure 15, where four friction torque is considered for the model. The first friction torque,  $T_{f1}$ , is due to the wave generator ball bearing, which can be modelled as a combination of static and viscous friction. The second friction,  $T_{f2}$ , corresponds to the gear-tooth meshing friction, and can be modelled as a Stribeck, static and friction. The friction denoted with  $T_{st}$ , is due to the structural damping of the flexspline, where the nature of this should be captured through identification, and the last friction is due to output ball bearing which can be modelled by a static plus viscous friction model.

The governing equations between each two nodes can be written as following:

$$\begin{cases} \theta_{wg} = \theta_{nwg} \\ T_{wg} = T_{nwg} + T_{v1}\dot{\theta}_{wg} + T_{s1}\text{sign}(\dot{\theta}_{wg}) \end{cases} \quad (40)$$

$$\begin{cases} \theta_{nwg} = N \cdot \theta_{nfs} \\ T_{nwg} = \frac{1}{N}T_{nfs} + T_{f2} \end{cases} \quad (41)$$

$$\begin{cases} T_{nfs} = T_{cfs} \\ T_{nfs} = K_1(\theta_{nfs} - \theta_{fs}) + K_2(\theta_{nfs} - \theta_{fs})^3 + T_{st} \end{cases} \quad (42)$$

$$\begin{cases} \theta_{cfs} = \theta_{fs} \\ T_{fs} = T_{cfs} - T_{v3}\dot{\theta}_{fs} - T_{s3}\text{sign}(\dot{\theta}_{fs}) \end{cases} \quad (43)$$

where the friction model for the gear-tooth meshing can be simple static friction and viscous damping, or the model of Hess and Soom [16], or Tustin model [2], as follows:

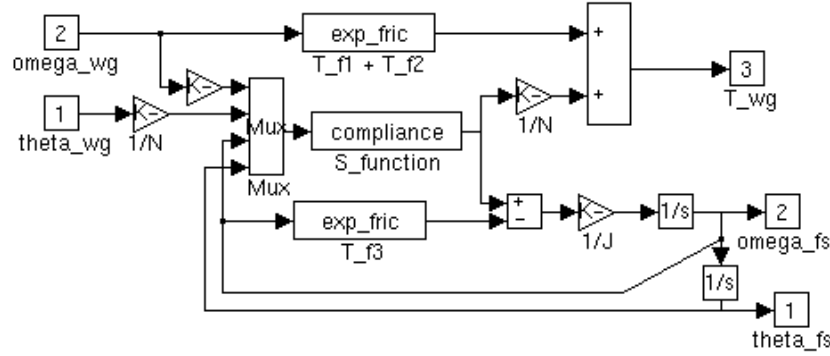
$$T_{f2} = \begin{cases} T_{v2}\dot{\theta}_{wg} + T_{s2}\text{sign}(\dot{\theta}_{wg}) \\ T_{v2}\dot{\theta}_{wg} + T_{s2}\text{sign}(\dot{\theta}_{wg}) + T_{ss1}\frac{\text{sign}(\dot{\theta}_{wg})}{1 + \left(\frac{\dot{\theta}_{wg}}{T_{ss2}}\right)^2} \\ T_{v2}\dot{\theta}_{wg} + T_{s2}\text{sign}(\dot{\theta}_{wg}) + T_{ss1}\text{sign}(\dot{\theta}_{wg})e^{-\left(\frac{\dot{\theta}_{wg}}{T_{ss2}}\right)^2} \end{cases} \quad (44)$$

Different models for structural damping,  $T_{st}$ , are proposed by researchers. One main behavior of the compliance is the hysteresis in the torsion curve, which can be modelled by Dahl friction, [9], by other mathematical model for hysteresis like Preisach model, [20], or by other form of velocity dependent frictions. The details of the corresponding models will be explained in the identification section, where by experiment different models will be examined to approximate the input output relations.

Figure 17 illustrates the simulation block of harmonic drive and the output load. The output angular displacement of harmonic drive actuates the output load,  $J_{out}$ , where in free load situation,

$$J_{out}\ddot{\theta}_{fs} = T_{fs} \quad (45)$$

There are two blocks used in the simulation which are written in C and linked to the Simulink using Cmx compiler. Compliance block has four inputs,  $\dot{\theta}_{nfs}$ ,  $\theta_{nfs}$ ,  $\dot{\theta}_{fs}$ , and  $\theta_{fs}$ , and the torsion torque,  $T_{cfs}$ , as output. In calculating this torsion the cubic model of stiffness and a velocity dependent model for structural damping is used. The

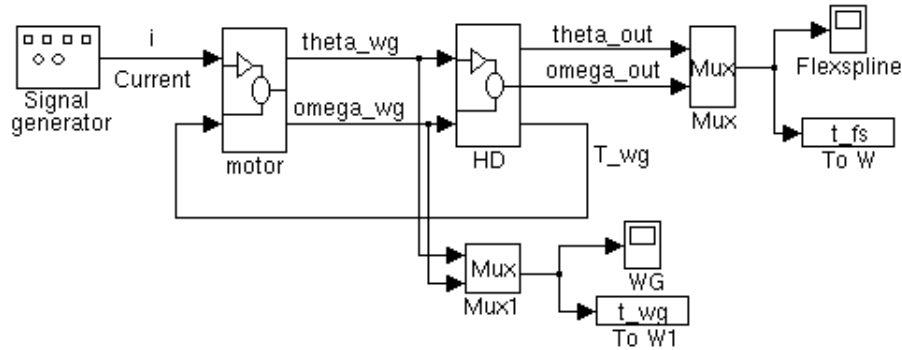
FIGURE 16. *Harmonic drive model simulated on Simulink*

friction block is the same as the friction block in the motor, and refer to the details explained in Section 2.1.1 a smoothing method is used to avoid chattering velocity. A full model of viscous plus Coulomb plus Stribeck friction is used in Figure 17 friction block, where exponential model is used for the Stribeck part and all friction components are considered to have velocity direction dependent coefficient.

### 2.3. Overall System Modelling and Simulation.

The testbed consist of signal generator, DC motor, harmonic drive, and output load. We modelled the system for two special applications, free-load and locked-load motion. Figure 17 illustrates the free load case, in which the motor and harmonic drive blocks (Figures 6 and 16 respectively) are used in connection to a signal generator. The displayed outputs are the flexspline and wave generator angular position and velocity, which will be displayed online on the scopes as well as logged into the Matlab workspace vectors,  $t_{out}$ , and  $t_{in}$  respectively.

The locked load case is similar to the free load simulation, while the output position and velocity is forced to be zero, as illustrated in Figure 18. In this case the output inertia, and load don't come into the picture. These two simulation routines are the main tool for further simulation verification and controller design.

FIGURE 17. *Overall System model simulated on Simulink: Free load case*

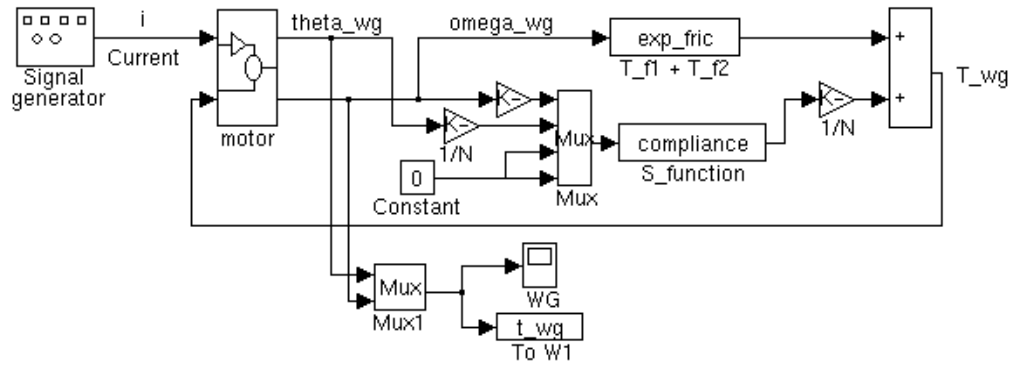


FIGURE 18. Overall System model simulated on Simulink: Locked load case

### 3. DC-MOTOR IDENTIFICATION

In this section we discuss the parameter identification of the DC motor model used in the harmonic drive system. Although the mathematical model for the harmonic drive is more complicated than that of the DC motor, the identification problems are quite similar in nature. Moreover, it is easier to experiment on the DC motor, therefore, we will first apply the identification approach on the DC motor, analyse the results, understand the practical difficulties, and then apply the identification process on the harmonic drive.

#### 3.1. Introduction.

A key point in our identification process is that we use only one set of experiments to identify all the parameters together. In the literature there are some attempts to identify different parameters separately through applying carefully designed set of experiments. However, as Tuttle et al. observed, [27, 28], this is a difficult task, and for some parameters (harmonic drive friction and compliance) it is not feasible. This method is a unified method which can identify all the system parameters, provided the experiment inputs are *persistently exciting*. A persistently exciting input is an input where all the system components are contributing in the output. A chirp function or a composite of three or more harmonics can be used as such an input. Moreover, as mentioned in [2, 11, 22], the behaviour of friction in the low speed region is different than that in the high speed. Therefore, another low speed experiment is required to excite the stick-slip or Stribeck friction.

In this section we will first discuss the regression models of the DC motor, then introduce the simulations for an identification test and comparison of the different methods. Then the DC motor experiments will be outlined and the identification results discussed. Finally, the simulation result equipped with the identified parameters will be compared to the experimental results.

#### 3.2. Linear Regression Model.

As explained in Section 2.1, the mathematical model for the DC motor powered with a servo amplifier can be represented by

$$\tau_m = \tau_i + \tau_f + \tau_o \quad (46)$$

where  $\tau_m$  is the motor torque produced by the amplifier current,  $\tau_i$  is the inertial torque,  $\tau_f$  is the friction torque, and  $\tau_o$  is the output torque. It can be shown that,

$$\tau_m = K_m \dot{\theta} \quad , \quad \tau_i = J_m \ddot{\theta} \quad , \quad \tau_o = \text{const. or } 0 \quad (47)$$

where  $K_m$  is the torque constant, and  $J_m$  is the rotor inertia. The friction torque can be represented by different models. To have a linear regression model we consider only static and viscous friction as illustrated in Figure 19, which can be expressed as,

$$\tau_f = T_v \dot{\theta} + T_s \text{sign}(\dot{\theta}) \quad (48)$$

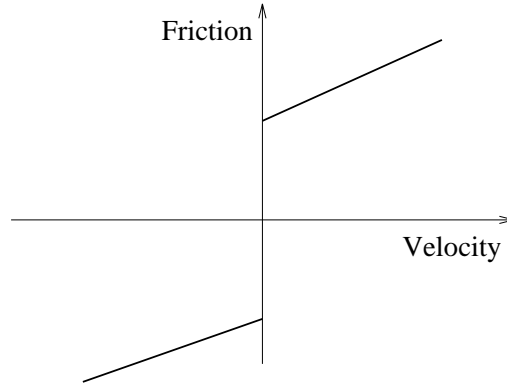


FIGURE 19. *The friction model consists of static and viscous friction*

where  $T_v$  is the viscous friction coefficient and  $T_s$  is the static friction coefficient. Finally the system model will be,

$$J_m \ddot{\theta} + T_v \dot{\theta} + T_s \text{sign}(\dot{\theta}) = K_m i - \tau_o \quad (49)$$

Notice that the model is nonlinear with respect to the angular displacement; however, considering the identification parameters,  $\theta$ , as:

$$\theta = [K_m, J_m, T_v, T_s] \quad (50)$$

The model is linear in  $\theta$ , provided the angular velocity, angular acceleration, servo amplifier current, and the output torque are known. However, in practice only angular displacement or angular velocity is measured and angular acceleration is not known. As we mentioned in Section 1.3.4 there are different methods to derive the acceleration from the velocity and shown that for nonlinear system the best way is to numerically differentiate the filtered signal, where a fifth order Butterworth filter, by zero-phase distortion routine is used to filter the signal.

The linear regression model can be summerized to,

$$\begin{bmatrix} i_f^0 & -\dot{\theta}_{fd}^0 & -\dot{\theta}_f^0 & -\text{sign}(\dot{\theta}_f^0) \\ i_f^1 & -\dot{\theta}_{fd}^1 & -\dot{\theta}_f^1 & -\text{sign}(\dot{\theta}_f^1) \\ i_f^2 & -\dot{\theta}_{fd}^2 & -\dot{\theta}_f^2 & -\text{sign}(\dot{\theta}_f^2) \\ \vdots & \vdots & \vdots & \vdots \\ i_f^m & -\dot{\theta}_{fd}^m & -\dot{\theta}_f^m & -\text{sign}(\dot{\theta}_f^m) \end{bmatrix} \begin{bmatrix} k_m \\ J_m \\ T_v \\ T_s \end{bmatrix} = \begin{bmatrix} \tau_o^0 \\ \tau_o^1 \\ \tau_o^2 \\ \vdots \\ \tau_o^m \end{bmatrix} \quad (51)$$

where  $\dot{\theta}_f$  is the digitally filtered angular velocity,  $\dot{\theta}_{fd}$  is the numerical derivative of  $\dot{\theta}_f$ , which serves as the angular acceleration, and the measured signals are logged as vectors with  $M + 1$  rows.

### 3.3. Nonlinear Regression Model.

The nonlinear model of DC motor can be derived by considering complete models of the friction. At low speed the behavior of friction cause the system to exhibit stick slip. This phenomena determines the lowest sustainable speed, and the shortest governable motion; therefore its dynamics is worthwhile to be understood. Space permits here only a brief outline of the new modelling achievements of this kind

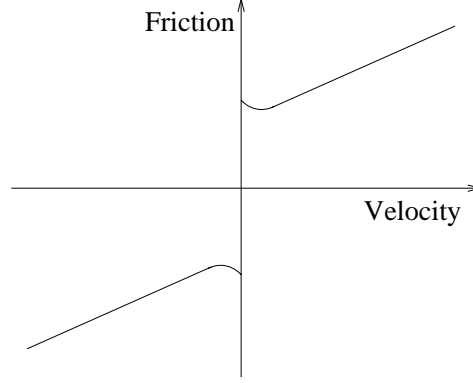


FIGURE 20. *The friction model consists of static, viscous, Stribeck friction*

of friction, and a more complete discussion can be found in [2, 16, 22]. Figure 20 illustrates the friction shape as a function of velocity. A few mathematical models are developed for the friction. Hess and Soom, [16], proposed the following form,

$$\tau_f = T_s \text{sign}(\dot{\theta}) + T_v \dot{\theta} + T_{ss1} \frac{1}{1 + (\frac{\dot{\theta}}{T_{ss2}})^2} \text{sign}(\dot{\theta}) \quad (52)$$

Armstrong, [1] employed Tustin's exponential model for friction which can be characterized as:

$$\tau_f = T_s \text{sign}(\dot{\theta}) + T_v \dot{\theta} + T_{ss1} e^{-\left(\frac{\dot{\theta}}{T_{ss2}}\right)^2} \text{sign}(\dot{\theta}) \quad (53)$$

In this section we consider Hess and Soom model, Equation 52, because of its analytic tractability. The third term, in the friction captures the negative slope regime, which is caused due to partial fluid lubrication, and two coefficient  $T_{ss1}$  and  $T_{ss2}$  is required to model it.

From Equation 46 the dynamic model of the DC motor can be written as,

$$J_m \ddot{\theta} + T_v \dot{\theta} + T_s \text{sign}(\dot{\theta}) + T_{ss1} \frac{1}{1 + (\frac{\dot{\theta}}{T_{ss2}})^2} \text{sign}(\dot{\theta}) = K_m i + \tau_o \quad (54)$$

The new set of identification parameters  $\boldsymbol{\theta}$  is,

$$\boldsymbol{\theta} = [K_m, J_m, T_v, T_s, T_{ss1}, T_{ss2}] \quad (55)$$

and the nonlinear regression model is as follows:

$$\mathbf{f}(\boldsymbol{\theta}) = \begin{bmatrix} f^0(\boldsymbol{\theta}) \\ f^1(\boldsymbol{\theta}) \\ \vdots \\ f^m(\boldsymbol{\theta}) \end{bmatrix} = \mathbf{0} \quad (56)$$

where

$$f^i(\boldsymbol{\theta}) = J_m \dot{\theta}_f^i + T_v \dot{\theta}_f^i + T_s \text{sign}(\dot{\theta}_f^i) + T_{ss1} \frac{1}{1 + (\frac{\dot{\theta}_f^i}{T_{ss2}})^2} \text{sign}(\dot{\theta}_f^i) - K_m i_f^i - \tau_o^i \quad (57)$$





signals. The results are illustrated in Table 1. In both case a composite of three harmonics are applied as the input current. The result of linear regression model is close to the nominal values, and by decreasing the variance of the noise we get better results. However the Stribeck parameters are far off identified compared to the nominal values. This can be rationalized by reconsidering the input signal which has sinusoidal components. Stribeck friction occurs at low speeds, therefore, this input signal is not persistently exciting for Stribeck friction. We applied a low velocity saw-tooth signal as input and redone the identification process, and get the following results,

$$\begin{aligned} T_{ss1} &= 0.245 \quad (24 \times \text{Real}) \\ T_{ss2} &= 0.45 \quad (10 \times \text{Real}) \end{aligned} \quad (58)$$

However, the other parameters are estimated inaccurately. That is because this input can not excite them. This result implies that to get reasonable results for all the parameters it is better to divide the identification problem into two parts. First find the parameters which can be found by the linear regression model. Then plug them into the nonlinear regression model as known parameter and obtain the other ones. This partition results in

$$\begin{aligned} T_{ss1} &= 0.05 \quad (5 \times \text{Real}) \\ T_{ss2} &= 3.5 \times 10^{-3} \quad (0.07 \times \text{Real}) \end{aligned} \quad (59)$$

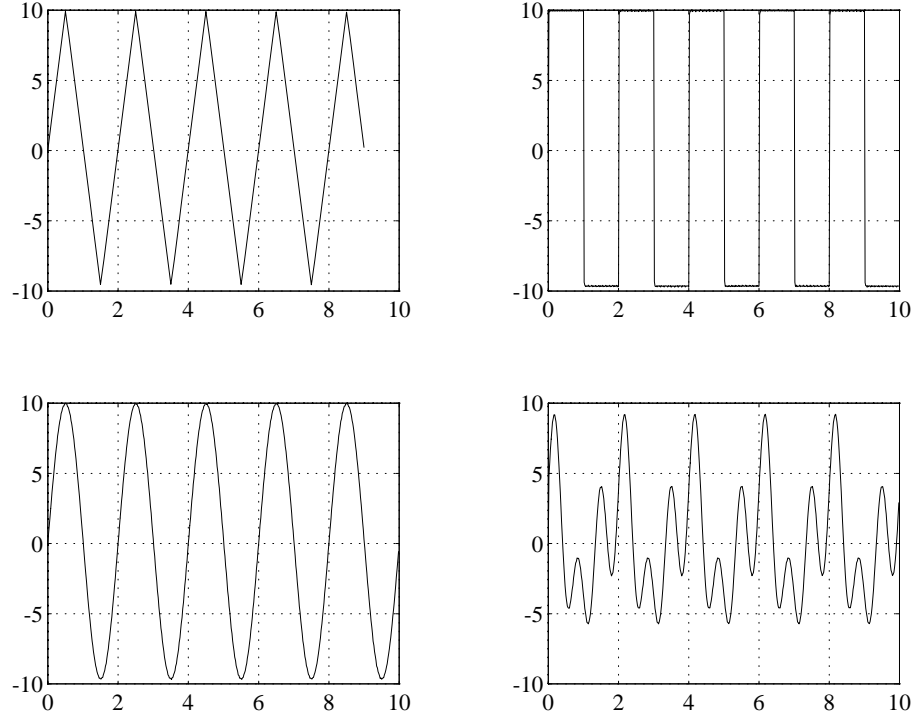
which gives better result for the first parameter but still not quite accurate result for the second parameter. This may be due to this fact that the second parameter of Stribeck friction does not affect the simulation output. To show this, a series of simulation were executed and it is observed that this parameter does not effect the output of the system; therefore, the identification result can not target the right parameter. From a control point of view this malfunction is not critical, since we require a model to capture the behaviour of the system, and as far as the the input output behavior can be estimated within a certain error limits, the amount of individual parameters are not important. This leads us to believe that the partition method of linear and nonlinear regression model for identification can be used for real system.

### 3.5. Experiments Outline.

Two set of experiments are considered for the DC motor identification. Four different signals are selected for each set. Figure 22 illustrates the high velocity signals which will be used for linear regression model. The forth signal in this set is composite of three sinusoid as following,

$$y(t) = \cos(t) + 0.5 \sin(2t) + \sin(3t) \quad (60)$$

The low velocity signals are saw-tooth signal like the first signal illustrated in Figure 22 with lower amplitude. These signals will be used for nonlinear regression model. These signals are applied through a software to the servo amplifier. The real current input to the motor and the output angular velocity of the system are measured and stored for the identification process. Figure 23 illustrated the measured input and output signals of a typical experiment (composite input). The variance of

FIGURE 22. *Different current input signals*

noise is less than %0.5 of maximum peak of signal for this case but this will increase two %2 for low velocity signals.

### 3.6. Final Identification Results.

Similar to Section 3.4, identification process is applied to the real input-output signals. The only difference is that there is no output torque applied to the motor; therefore, the linear regression model simplifies to,

$$\mathbf{A}\boldsymbol{\theta} = \mathbf{0} \quad (61)$$

In order to get the non scaled value of the parameters in this case we should supply one of the parameters. The motor inertia is supplied, since it is the one given with

	$J_m$	$K_m$	$T_v$	$T_s$
Saw-tooth	$4.376 \times 10^{-5}$	$4.33 \times 10^{-2}$	$3.42 \times 10^{-5}$	$1.31 \times 10^{-2}$
Square	$4.376 \times 10^{-5}$	$4.25 \times 10^{-2}$	$2.94 \times 10^{-5}$	$1.29 \times 10^{-2}$
Sine	$4.376 \times 10^{-5}$	$4.26 \times 10^{-2}$	$4.22 \times 10^{-5}$	$1.22 \times 10^{-2}$
Composite	$4.376 \times 10^{-5}$	$4.27 \times 10^{-2}$	$4.75 \times 10^{-5}$	$1.08 \times 10^{-2}$
Final Decision	$4.376 \times 10^{-5}$	$4.27 \times 10^{-2}$	$4.0 \times 10^{-5}$	$1.2 \times 10^{-2}$

TABLE 2. *Least square results of linear regression model for the DC motor*

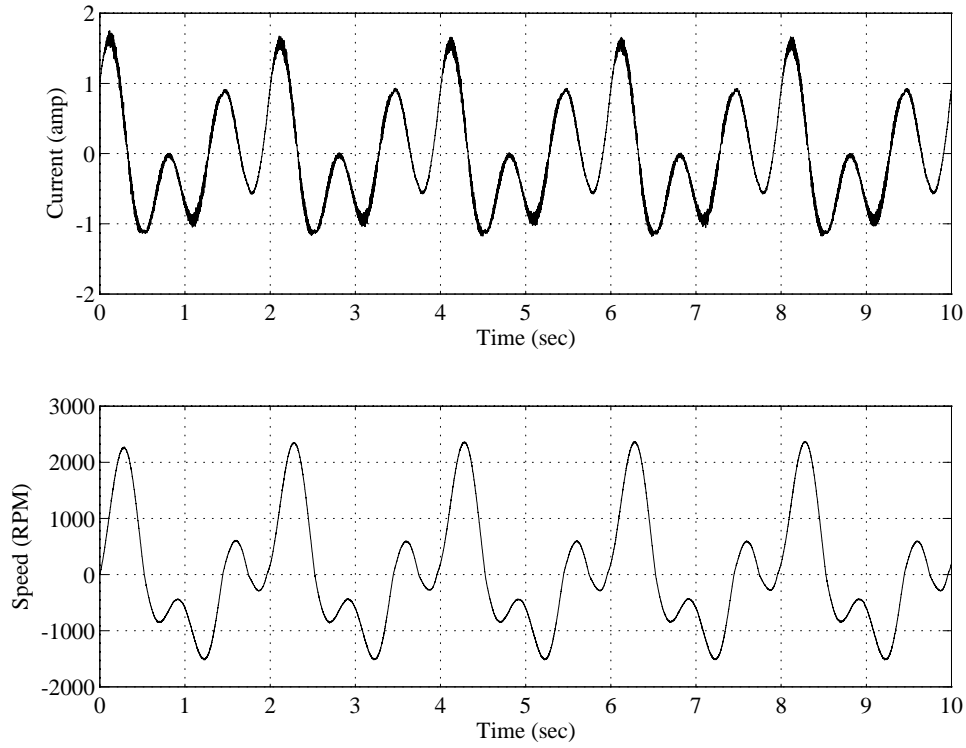


FIGURE 23. *Typical experimental input-output signals*

most accuracy in the technical specification. Four different pair of input-output result in slightly different values for the parameters. These results are given in Table 2. Out of the four observation a final value is decided for every parameter. This final value is provided for the nonlinear regression model and the resultant values for Stribeck friction observed to be very small and negligible. This confirms the manufacturer's claim that the slip stick friction for the DC motor is negligible.

### 3.7. Simulation and Experiment Comparison.

To verify the identification results, the measured input signal is used as an input to the simulation and the simulation output is compared to the experiments. This approach will not only verify the identification parameters, but also give some insight into the physical correspondence of the parameters.

Figures 24 and 25 illustrate the comparison of simulation and experiments for low and high velocities. the following observation can be done on the comparison results.

- Low friction experiments

- 1: The behavior of system for positive velocity is different than that for the negative velocity. In fact the speeds the rotor reaches is more in negative direction than that in positive direction. This can be rationalized as having different friction characteristics depending on velocity direction.

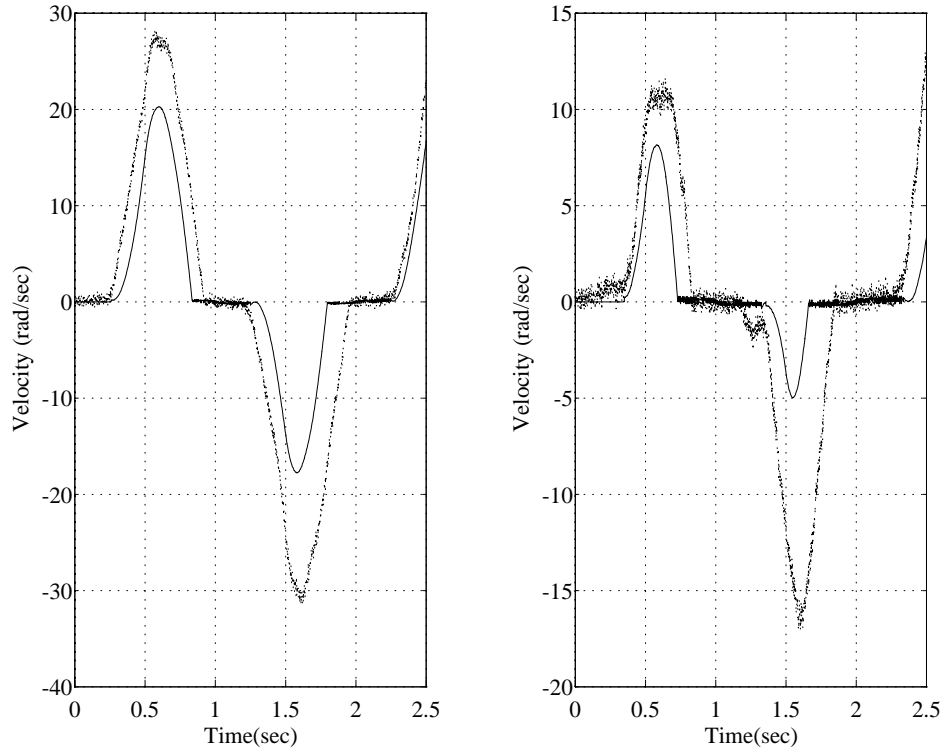


FIGURE 24. *Comparison of simulation to experiments for low velocity input*

- 2: The break away points in the simulation occurs later than that in experiments. Also the break away points in experiments depend on velocity direction.
  - 3: In the second graph of Figure 24 some dynamics are observed for the negative breakaway portion of the motion. This can be rationalized by existence of Stribeck friction. However, this does not occur in the other experiments and looks to be a local friction property which is not identifiable by the identification process.
  - 4: The peak positive velocity in the second graph of Figure 24 happen to be exceptionally flat, which again is a local property and can not easily be modelled.
- High velocity experiments
    - 1: Different friction behavior for positive and negative velocity.
    - 2: At positive velocity the identified friction should be more, while at negative velocity it should be less.

We conclude that the static friction which plays an important role in low velocities should have lower amount than that which is obtained from identification. Also there is a requirement of having two different static friction coefficient depending on the velocity direction. At high velocity viscous friction is more important, and

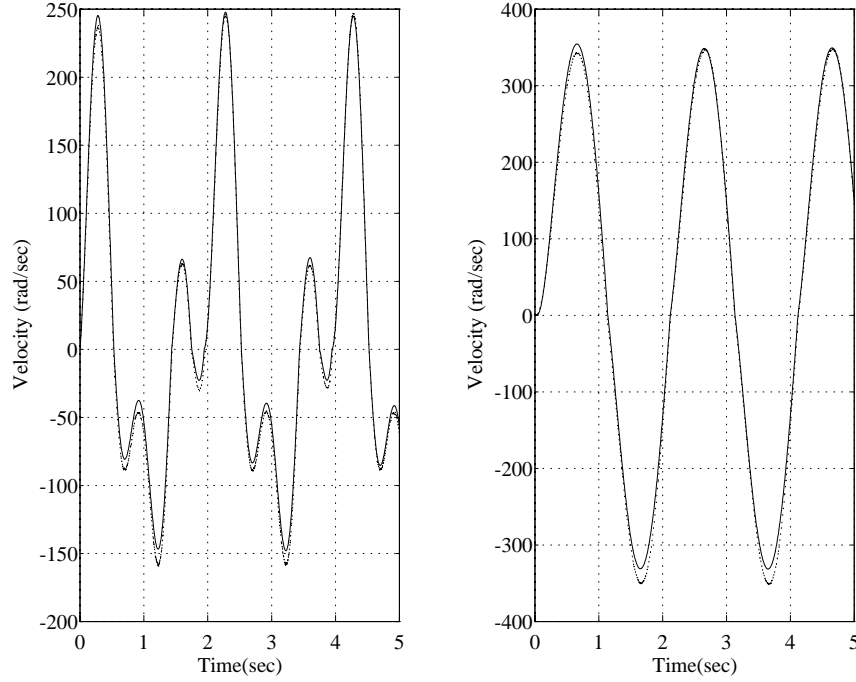


FIGURE 25. *Comparison of simulation to experiments for high velocity input*

therefore, it should be modelled with two different velocity direction coefficients. Also the value of positive viscous coefficient is anticipated to be more than the current identified parameter, while the negative viscous coefficient might be less than that. The Stribeck friction exist but because it is locally observed it is hard to put it into a consistent model.

To obtain a better match we applied the following modification into the regression models and processed the identification scheme on it. The following equation is capable of including different static and viscous friction with respect to the velocity direction.

$$J_m \ddot{\theta} + T_{v_n} u_{-1}(-\dot{\theta}) \dot{\theta} + T_{v_p} u_{-1}(\dot{\theta}) \dot{\theta} + T_{s_n} u_{-1}(-\dot{\theta}) \text{sign}(\dot{\theta}) + T_{s_p} u_{-1}(\dot{\theta}) \text{sign}(\dot{\theta}) + T_{ss1} \frac{1}{1 + (\frac{\dot{\theta}}{T_{ss2}})^2} \text{sign}(\dot{\theta}) = K_m i + \tau_o \quad (62)$$

in which the subscript  $n$  denotes the negative velocity direction coefficient, while  $p$  denotes positive velocity direction coefficient, and  $u_{-1}(x)$  is defined similar to unit step function but not in the time domain:

$$u_{-1}(x) = \begin{cases} 1 & \text{if } x > 0 \\ 0 & \text{if } x \leq 0 \end{cases} \quad (63)$$

Similar linear and nonlinear regression models can be constructed with this new formulation and the identification process applied for them. Table 3 illustrates the results for the new linear regression model, while the nonlinear regression model

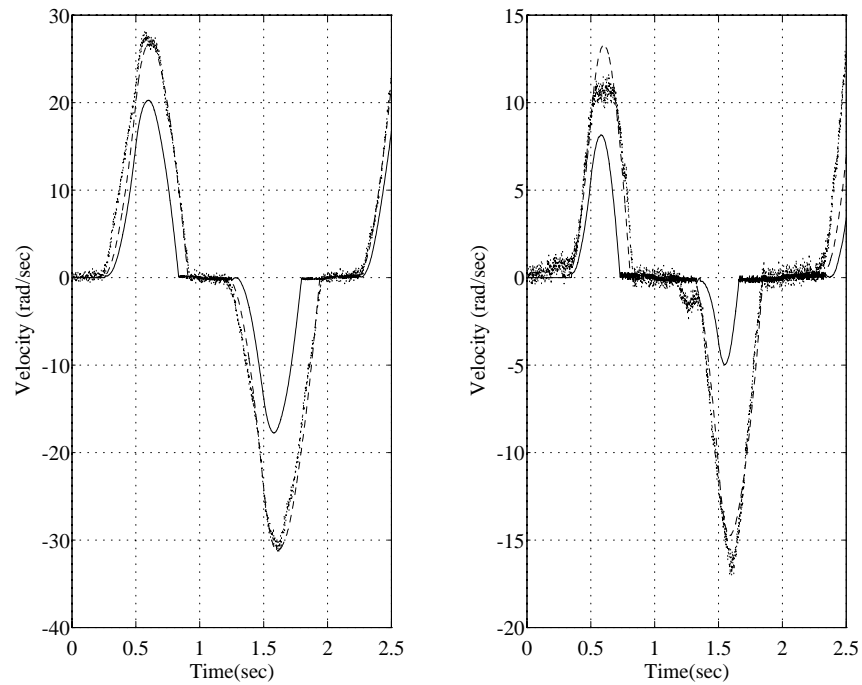


FIGURE 26. Comparison of simulation using identified parameter and modified identified parameters to experiment for low velocity input

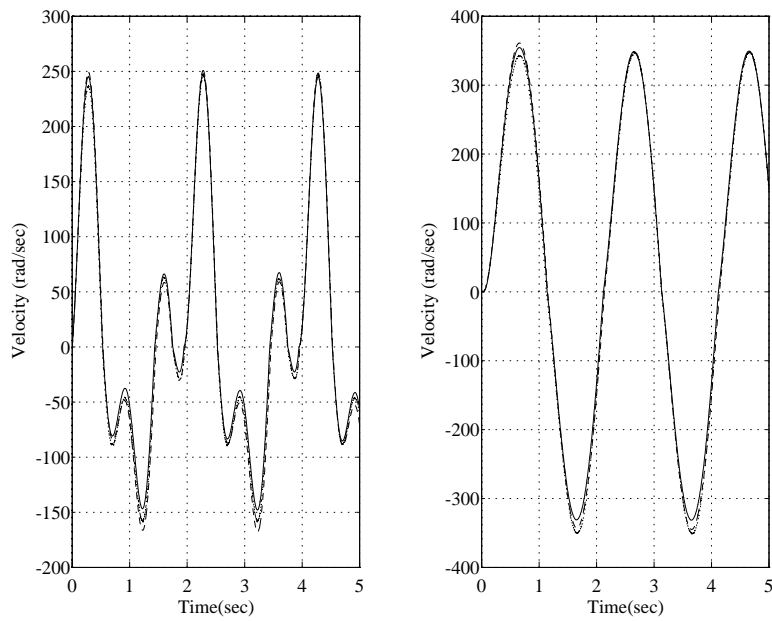


FIGURE 27. Comparison of simulation using identified parameter and modified identified parameter to experiment for high velocity input

again results in zero coefficient for Stribeck friction. The final decision is consistent with the observations made on previous identification verification. Figures 26, and 27 give a comparison of the experiment and simulation using both identified parameters obtained from Section 3.6 and modified regression model given by Equation 62. The dotted signal corresponds to the experiment, the solid line denotes the simulation result using first set of identified parameters, and the dashed line denotes the simulation result using modified parameters. For low velocity experiments the model matching is accomplished by the modified model, while there is still little discrepancy observed for high velocity experiments. To match the parameters for high velocity experiments some trial and error tuning is forwarded to gets better results, but it is observed that by changing the viscous friction coefficient better matching is obtained for some experiments but not for all experiments. Finally, the final decision parameters given in Table 3 is a good trade off for matching of all the experiments, and although the worst normalized deviation is about 23%, Figures 26, and 27 are a good indicator of this success.

	$K_m$	$T_{v_n}$	$T_{v_p}$	$T_{s_n}$	$T_{s_p}$
Saw-tooth	$4.34 \times 10^{-2}$	$3.26 \times 10^{-5}$	$3.63 \times 10^{-5}$	$1.28 \times 10^{-2}$	$1.33 \times 10^{-2}$
Square	$4.25 \times 10^{-2}$	$2.69 \times 10^{-5}$	$3.22 \times 10^{-5}$	$1.28 \times 10^{-2}$	$1.29 \times 10^{-2}$
Sine	$4.26 \times 10^{-2}$	$4.12 \times 10^{-5}$	$4.32 \times 10^{-5}$	$1.16 \times 10^{-2}$	$1.25 \times 10^{-2}$
Composite	$4.27 \times 10^{-2}$	$5.29 \times 10^{-5}$	$4.37 \times 10^{-5}$	$1.02 \times 10^{-2}$	$1.16 \times 10^{-2}$
Final Decision	$4.275 \times 10^{-2}$	$4.2 \times 10^{-5}$	$4.2 \times 10^{-5}$	$1.0 \times 10^{-2}$	$1.1 \times 10^{-2}$
Std/Final	0.82%	23.3%	11.5%	9.0%	5.7%

TABLE 3. *Least-square results of modified linear regression model for the DC motor*

.



## 4. HARMONIC DRIVE IDENTIFICATION

Similar to the Section 3, in this section the parameter identification of Harmonic Drive model will be presented. This section is divided into two parts, compliance and friction identification. In each part different regression models will be considered and least square results will be presented. Then the result of the final estimated model will be validated by experiments.

### 4.1. Introduction.

Harmonic drive is a special designed gear transmission, in which a flexible element named flexspline, made this transmission unconventional. Due to the special design of this transmission, modelling of the friction and the compliance of the drive is very important. The identification procedure will deal with identifying these parameters. Individual researcher [17, 19, 21, 27] attempted to identify the harmonic drive parameters by designing careful experiments to extract each one of parameters from one experiment. However, some of the characteristics of harmonic drive are so mixed, which are not possible to identify them separately. Tuttle, [27], tried to decouple the inherent mixed up between the friction and stiffness by arranging an ideal static test, which proves to be very difficult in practice.

We propose an identification procedure like what applied for the DC motor to obtain all the parameters at once. In this method there is no need to design careful experiments, and the only requirement is that the inputs are persistently exciting. The quantities which are measurable are the input motor current and angular velocity, and the torque transmitted through the flexspline, and output angular position. This torque measurement is accomplished using the compliance of the flexspline itself, where its idea is given first by Hashimoto et al. [14, 15]. This torque sensing technique has two major benefits. First we don't add another flexible element into the system, second, it measures the real torque transmitted through the flexspline; therefore, it is not contaminated with any external source of friction. The output position is measured via an encoder; therefore, direct differentiation to gain velocity or acceleration is not efficient. To do that a Kalman filter is designed to estimate the output velocity and acceleration. Let us look at the identification problem in the context of the available measurements.

### 4.2. Harmonic Drive Compliance.

To have a persistently exciting experiment for harmonic drive compliance, a locked load experiment is candidated. In locked load case maximum torque of motor can be applied to the flexspline to have maximum deformation. Considering the complete model of harmonic drive discussed in Section 2.2.3 illustrated in Figure 15, the measured quantities are, the wave generator velocity,  $\dot{\theta}_{wg}$ , and the flexspline torque,  $T_{n_{fs}}$  which is identical to  $T_{c_{fs}}$ . By integrating the angular velocity  $\dot{\theta}_{wg}$  angular position of the motor  $\theta_{wg}$ , can be derived accurately. On the other hand, the measured torque is the result of the torsion and structural damping of the flexspline. Tuttle et al., [28], and Kircanski et al., [18] have proposed cubic stiffness model for the harmonic drive system. However, they didn't proposed any specific model to capture structural

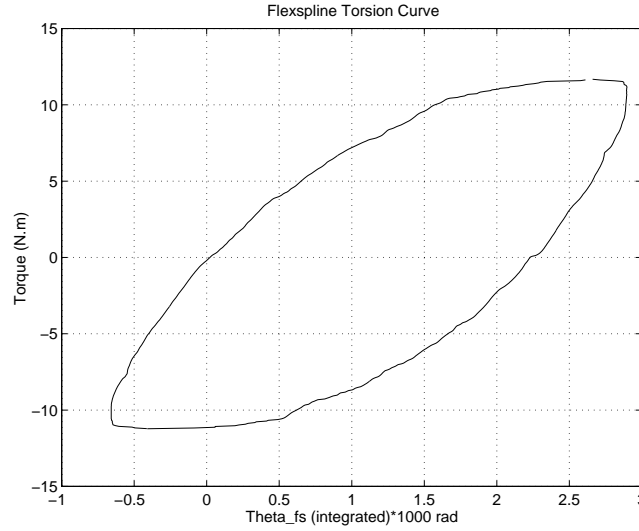


FIGURE 28. *Flexspline measured torsion in locked load experiment, which possess hysteresis*

damping. The structural damping of the flexspline cause hysteresis to the torsion curve as illustrated in Figure 28.

Refer to Equation 43, the torsion is compound of the stiffness and structural damping. For Locked load experiment,  $\theta_{fs} = 0$ ; therefore this equation simplifies to

$$T_{n_{fs}} = K_1 \theta_{n_{fs}} + K_2 \theta_{n_{fs}}^3 + T_{st} \quad (64)$$

where  $T_{n_{fs}}$  is the measured torque,  $T_{st}$  is the structural damping and  $\theta_{n_{fs}} = \frac{1}{N} \theta_{wg}$ . Many different models are proposed to capture the hysteresis behavior of structural damping. Macki et al. [20], give a very good comparison of different hysteresis models. In this paper, Hysteresis from a mathematical point of view is discussed, here the results can characterize magnetic or mechanical hysteresis. Dahl [9], investigated solid friction in mechanical vibrating systems, and proposed a mathematical model for that kind of friction. Later, Bliman [6] showed that Dahl friction model can be seen as a hysteresis operator. The original model of Dahl friction are as follows:

$$\dot{T} = \sigma \dot{\theta} \left| 1 - \frac{T}{T_c} \text{sign}(\dot{\theta}) \right|^i \text{sign}(1 - \frac{T}{T_c} \text{sign}(\dot{\theta})) \quad (65)$$

where  $\sigma$ ,  $T_c$ , and  $i$  are model constants which should be identified. It is clear that this model is a dynamic model, since the first derivative of the friction is related to the velocity and the friction torque itself. There is a modified version of Dahl's model, perhaps first discussed by Threlfall [26], in which  $i = 2$ . In this case Equation 65 will simplify to,

$$\dot{T} = \beta \dot{\theta} \left( T - T_c \text{sign}(\dot{\theta}) \right)^2 \quad (66)$$

There is another model of hysteresis worthwhile explaining here from literature, namely Duhem Model [20]. the formulation of this model is somewhat close to Dahl's

model (Equation 65):

$$\begin{cases} \dot{T} = a|\dot{\theta}| \left( T - \phi(\dot{\theta}) \right) + b\dot{\theta} \\ \phi(\dot{\theta}) = K_0 + K_1\dot{\theta} + K_2\dot{\theta}^2 + K_3\dot{\theta}^3 \end{cases} \quad (67)$$

where  $\phi(\dot{\theta})$  is an arbitrary shape function which can be a third order polynomial as shown in Equation 67. This model combines both the stiffness and structural damping of the system into one formulation.

Although there exist a rich literature in the modelling the hysteresis, like Babuska, Bouc, Ishlinskii, Preisach, and Krasnoselskii hysteresis operators [20], it proves to be very difficult to have a promising estimate of the harmonic drive compliance hysteresis, using these models. Another velocity dependent model is proposed, which better captures the structural damping hysteresis for harmonic drive. This model is a static model in the form of:

$$T = T_{st}|\dot{\theta}|^\alpha \text{sign}(\dot{\theta}) \quad (68)$$

where  $T_{st}$  is the damping coefficient and  $\alpha$  is the velocity exponent in the damping model. If  $\alpha$  is fixed the model will recast into a linear regression model. Although this model is simpler in structure than the dynamic models explained in Equations 65, 66 and 67, but since it represents the true relation of structural damping to the velocity, it proves to be a very effective model for structural damping.

#### 4.2.1. Regression Models.

From a locked load experiment we are able to measure the transmitted torque  $T_{cfs}$  and the motor input angular velocity  $\dot{\theta}_{wg}$ , and through integration a good estimate for angular position  $\theta_{wg}$ . To identify the stiffness and structural damping parameters, we first require a regression model. Since different models exist for structural damping, different regression models can be derived. Here we elaborate only two of them.

First consider the dynamic models for the structural damping for example modified Dahl model Equation 66, with general third order polynomial for stiffness. For this case we can formulate the identification model as:

$$\begin{cases} T_{cfs} = T_{meas} = T_{st} + T_{stiff} \\ T_{stiff} = K_0 + K_1\theta_{wg} + K_2\theta_{wg}^2 + K_3\theta_{wg}^3 \\ \dot{T}_{st} = \beta\dot{\theta}_{wg} \left( T_{st} - T_c \text{sign}(\dot{\theta}_{wg}) \right)^2 \end{cases} \quad (69)$$

The structural damping model is a differential equation. To get any regression model it is required to discretize this equation first, but since the differential equation is not linear, all discretization schemes are not applicable. Using the simplest method of backward difference, the differential equation can be discretized in the form of:

$$T_{st}[n] - T_{st}[n-1] = \beta\Delta T \dot{\theta}_{wg}[n] \left( T_{st}[n] - T_c \text{sign}(\dot{\theta}_{wg}[n]) \right)^2 \quad (70)$$

where  $\Delta T$  is the sampling time. Solving Equation 69 for  $T_{st}$  from the other side we get,

$$T_{st}[n] = T_{meas}[n] - T_{stiff}[n] = T_{meas}[n] - K_0 - K_1\theta_{wg}[n] - K_2\theta_{wg}^2[n] - K_3\theta_{wg}^3[n] \quad (71)$$

Equating  $T_{st}[n]$  in Equations 70 and 71, we get the nonlinear regression model for compliance of harmonic drive, namely:

$$f(\theta) = T_{meas}[n] - T_{stiff}[n] - T_{st}[n-1] - \beta \Delta T \dot{\theta}_{wg}[n] \left( T_{st}[n] - T_c \text{sign}(\dot{\theta}_{wg}[n]) \right)^2 = 0 \quad (72)$$

where  $\theta$  are the parameters of the model,

$$\theta = [K_0 \ K_1 \ K_2 \ K_3 \ \beta \ T_c]^T \quad (73)$$

This nonlinear regression model can be extended for other structural damping, and stiffness models, and different combinations can be tried to identify the parameters of the models. The details of these combinatory models will not presented here for sake of simplicity but the identified parameters will be explained later in this Section to establish which model can better capture the hysteresis behavior of system.

Considering Equation 68, we can get a linear regression model for the system. Similar to Equation 69, we can write,

$$\begin{cases} T_{cfs} = T_{meas} = T_{st} + T_{stiff} \\ T_{stiff} = K_0 + K_1 \theta_{wg} + K_2 \theta_{wg}^2 + K_3 \theta_{wg}^3 \\ \dot{T}_{st} = T_{st} |\dot{\theta}_{wg}|^\alpha \text{sign}(\dot{\theta}_{wg}) \end{cases} \quad (74)$$

By Fixing  $\alpha$ , we can get linear regression model as follows:

$$T_{meas} = K_0 + K_1 \theta_{wg} + K_2 \theta_{wg}^2 + K_3 \theta_{wg}^3 + T_{st} |\dot{\theta}_{wg}|^\alpha \text{sign}(\dot{\theta}_{wg}) \quad (75)$$

where the estimation parameter  $\theta$  will be,

$$\theta = [K_0 \ K_1 \ K_2 \ K_3 \ T_{st}]^T \quad (76)$$

Here we can use linear or cubic model for stiffness and get different linear regressions. An iterative method can be used to find the best value for  $\alpha$ , as well as using a nonlinear regression to estimate  $\alpha$ . The details and final estimated values will be given in next Section.

#### 4.2.2. Experimental Results.

Eleven different experiments is used for compliance identification. One experiment is enough to give a set of parameters, but having different experiments shows how the parameters deviate for different conditions. Like the experiment outline for DC motor identification the software can give four different signal types, namely sine, square, triangular, and composite (refer to Equation 60). Four experiment include these type of signals with 0.5 Hz frequency, and 50 % of input full power. To gain a complete loop of hysteresis, an asymmetric sine wave is added to the software signal generator. In this signal the amplitude of negative velocity signal is 1.2 times of that of positive velocity. This will compensate the velocity direction dependence of frictional losses. Figure 28 is result of this type of signal with 100% full power input. The rest of experiments are sine waves with different frequencies (0.2 - 1 Hz) and amplitudes (20% to 100%).

It is also important to have a good measure to compare the results of identification through different regression models, and with different experiment data. We considered two major measure here. First a quantitative comparison on the hysteresis

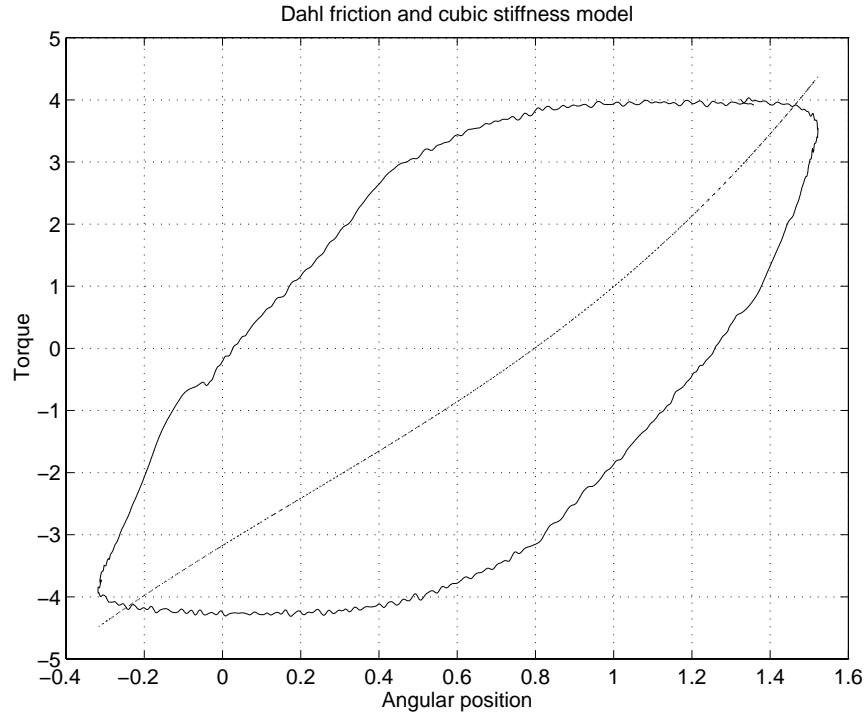


FIGURE 29. *Modified Dahl model for structural damping and cubic stiffness model compared to an experiment*

curve. This can be done by plotting the hysteresis curve resulting from experiment versus the estimated one. Although this measure is not accurate but can be used as a yes/no scale to throw away the unrealistic models. The second measure can be any kind of norm of error, which in this case we used an induced norm or  $\mathcal{H}_\infty$  norm of the error. This norm will give the normalized worst case error of each model, and is a better quantitative measure of the error for each model.

### Dynamic Model Results

As mentioned in Section 4.2.1 the dynamic models of structural damping form a nonlinear regression and iterative least square methods can be used to identify the parameters. Considering a cubic model for stiffness and modified Dahl model (Equation 66) for structural damping, this optimization problem is solved and the model parameters are identified. Figure 29 illustrates the real hysteresis loop of one experiment, versus the result of this model. Clearly, the identified parameters are not capable of introducing the hysteresis loop in this case. Different other dynamical models are tried as well, among them are Dahl model and modified Dahl model with different stiffness models, Duhem model, Ishlinskii model, and Preisach model. It is observed that all of them have similar characteristics as the one explained here, and therefore none of them can represent a realistic model for structural damping. It should be mentioned that, these models are all capable to model the hysteresis curve, but since they form a nonlinear regression, the identified parameters, obtained from these regression models, produce only a narrow hysteresis curve. This might be

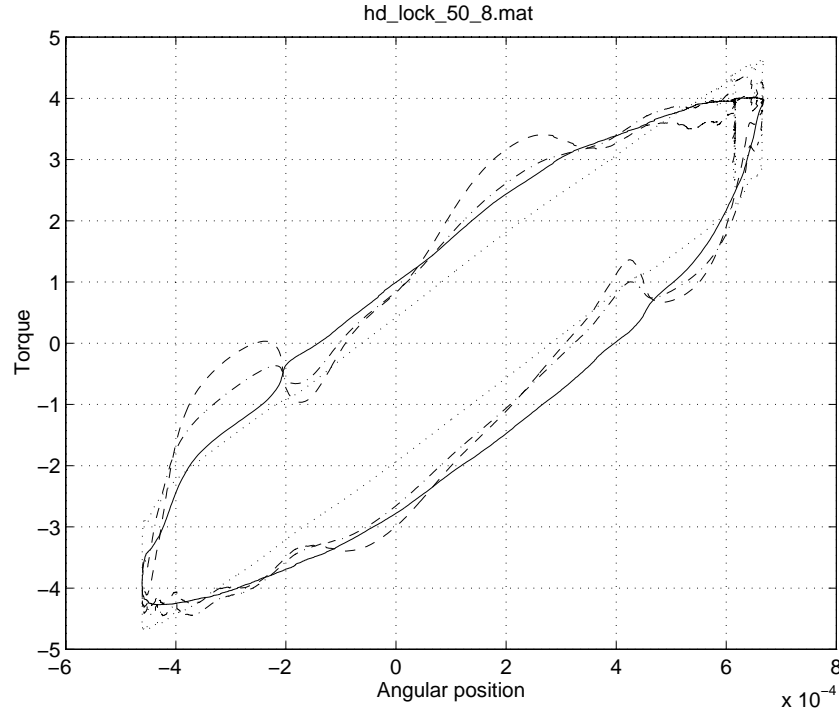


FIGURE 30. *Structural damping model, comparison of different velocity exponents; solid: experiment, dashed:  $\alpha = 1$ , dash-dotted:  $\alpha = 0.5$ , and dotted:  $\alpha = 0.1$*

caused by convergence of the optimization routine to a local optimum. By varying the model parameters manually, we observed wider hysteresis loops; however, since this is not a systematic way to find the model parameters we didn't resort to this method for finding the final parameters.

### Static Model Results

Returning to static models of structural damping, Equation 75 is the basis of identification. This model consists of a velocity dependent damping, where damping is proportional to an exponent of velocity. It is informative to explain how the idea of this model is developed. By comparing the position and velocity to the torque, we saw that there is a one to one correspondence between torque on one side and position and velocity on the other side. Naturally the simplest model, will presume a linear dependence of position and velocity. Figure 30 illustrates the estimation of this model versus the true hysteresis loop. The quantitative match of the model is fairly good, but there are a lot of unrealistic oscillation in the estimated curve. This oscillations are corresponding to the velocity oscillations. To reduce the amplitude of this oscillations, a model with a powered velocity with exponent less than one proved to help. An arbitrary exponent (i.e. 0.5) is tried and the improved result is shown in Figure 30. Decreasing the exponent to 0.1 will reduce the oscillations, however, the overall curve fitting is not good. To find an estimate of  $\alpha$ , an iterative method is forwarded, in which the hysteresis curves are qualitatively compared to each other

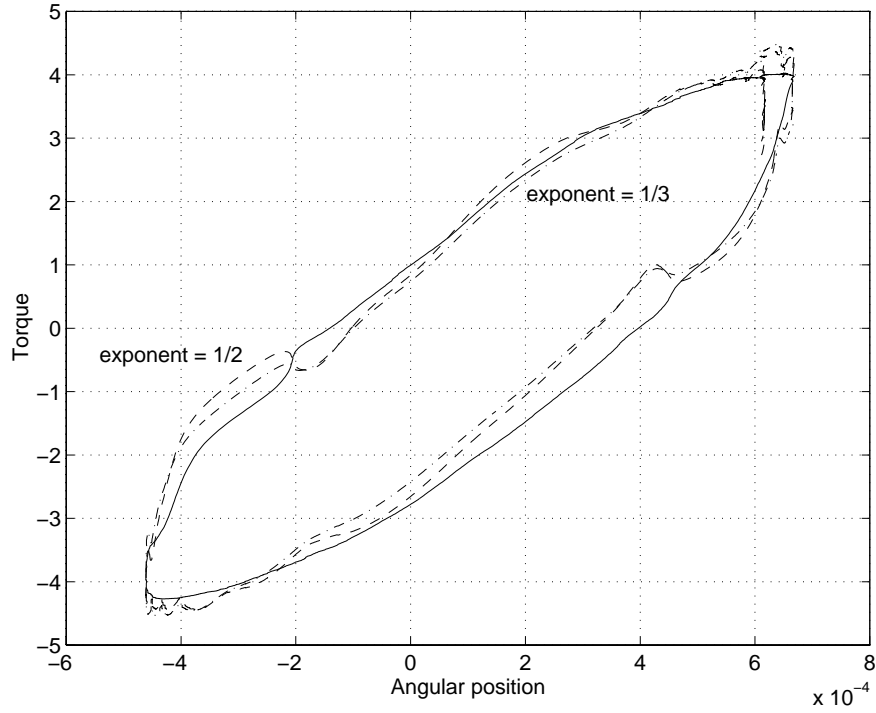


FIGURE 31. Comparison of two models with  $\alpha = \frac{1}{2}$  and  $\alpha = \frac{1}{3}$

to evaluate the models. Following this we observed that a range of  $\alpha = [0.25 \quad 0.6]$  give relatively good result.

To finalize the best value for  $\alpha$  two attempts has been done. First, we considered two values for  $\alpha$  namely  $\frac{1}{3}, \frac{1}{2}$  and pursued the linear regression models to obtain the stiffness and structural damping coefficients. For this case linear model for stiffness is used. Table 4 illustrates the least square results for four different experiments and these two values of  $\alpha$ . It is clear that the results would not be identical for all experiments; therefore, the average value can serve as a nominal value for each coefficient. The ratio of standard deviation to the average value give a normalized measure of error. Comparing this ratio for two preassigned values of  $\alpha$  shows that

	$\alpha = \frac{1}{3}$		$\alpha = \frac{1}{2}$	
<i>File</i>	$K_1$	$T_{st}$	$K_1$	$T_{st}$
100-8	$5.4227 \times 10^3$	33.776	$5.4610 \times 10^3$	85.965
50-8	$6.8188 \times 10^3$	11.736	$6.9288 \times 10^3$	35.328
50-1	$5.9653 \times 10^3$	21.458	$6.0779 \times 10^3$	61.365
50-7	$6.8006 \times 10^3$	18.111	$6.8971 \times 10^3$	46.061
Avg	$6.25 \times 10^3$	21.3	$6.34 \times 10^3$	57.2
Std/Avg	9.5%	38%	9.6%	33%

TABLE 4. Least square results of linear regression model of the harmonic drive for two velocity exponents  $\alpha = \frac{1}{2}$  and  $\alpha = \frac{1}{3}$

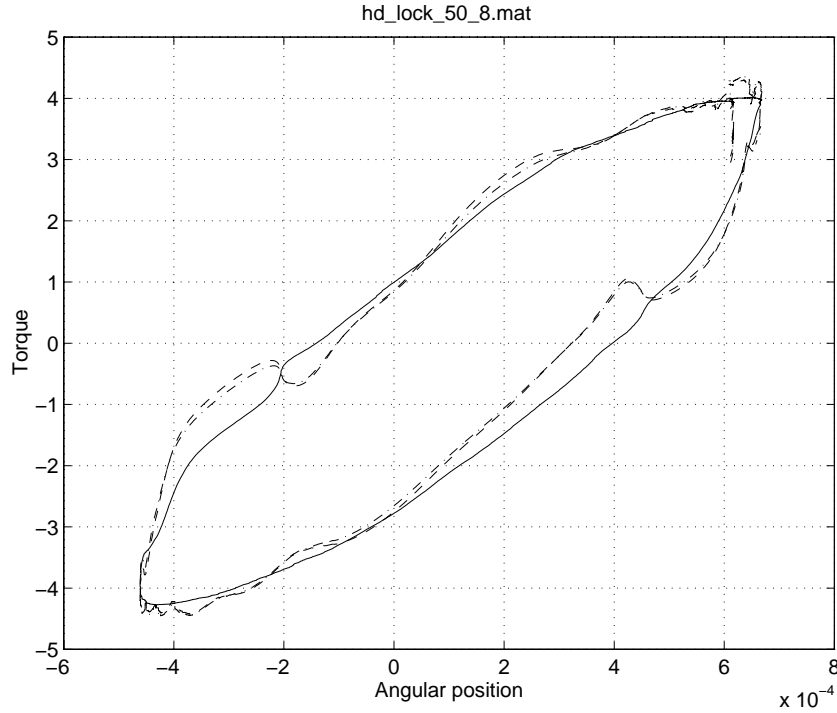


FIGURE 32. Comparison of hysteresis curve with optimal  $\alpha$  and  $\alpha = \frac{1}{2}$

the results are relatively close. Figure 31 also illustrates the real hysteresis loop versus the estimated ones, and qualitatively both model are good. To have a strict measure the nominal values for each  $\alpha$  is used to duplicate the experiment results, and  $\mathcal{H}_\infty$  norm of error is calculated for all eleven available experiments. It is observed that almost in all experiment the norm of error for  $\alpha = \frac{1}{2}$  is less than that for  $\alpha = \frac{1}{3}$ , and therefore,  $\alpha = \frac{1}{2}$  gives a better estimate.

This comparison is only between two values of  $\alpha$ . To obtain the best fit, we solved a nonlinear regression to estimate  $\alpha$  as well as the other coefficient. This has been examined on two different experiments, where the final estimated coefficients are given in Table 5. The optimal value for  $\alpha$  is close to  $\frac{1}{2}$  and varying by experiment. However, the norm of error for optimal  $\alpha$  and for that with nominal value  $\alpha = \frac{1}{2}$  are close. Figure 32 confirms the small difference between these two case as well. With

File	50-8	50-1
$K_1$	$6.9867 \times 10^3$	$6.0737 \times 10^3$
$T_{st}$	63.68	58.71
$\alpha$	<u>0.5224</u>	<u>0.4928</u>
Opt. Norm	4.223	10.817
Nom. Norm	4.472	10.820

TABLE 5. Least square results of non linear regression model of harmonic drive compliance



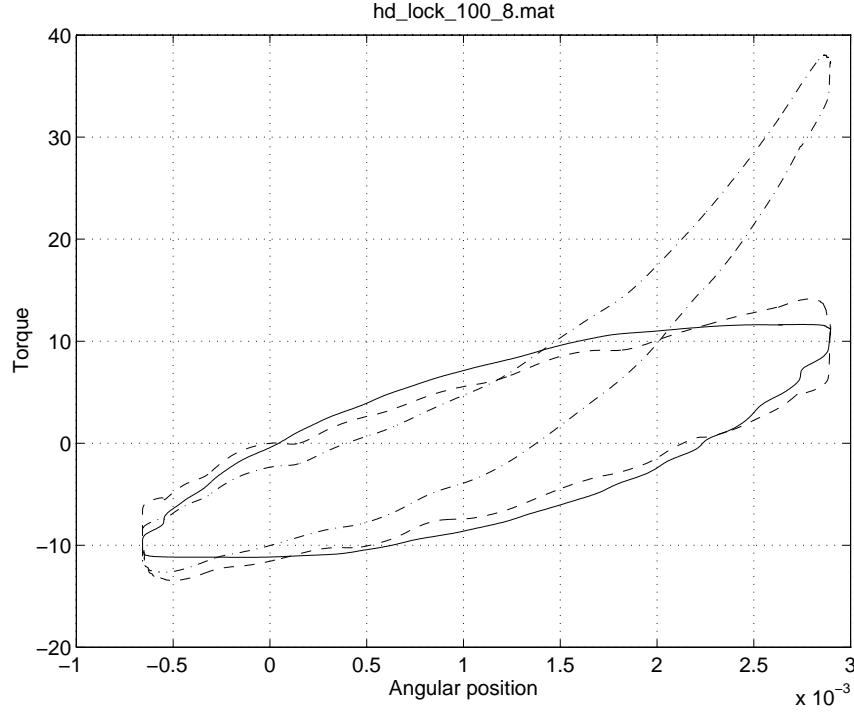


FIGURE 33. Comparison of the experimented hysteresis loop with the estimated cubic model of stiffness; solid: experiment, dashed: linear stiffness model, dash-dotted: cubic stiffness model

this result we can conclude that  $\alpha = \frac{1}{2}$  is a good and nearly optimal estimate for our model.

#### Cubic and linear model for stiffness

In the previous section we discussed different models of structural damping and only one model for stiffness. Through the literature, [28, 18], cubic stiffness is considered by different researcher, and this section is devoted to compare the linear and cubic stiffness models. From the last section we concluded that a velocity dependent model for structural damping with velocity exponent  $\alpha = \frac{1}{2}$ . Using this model we consider now linear and cubic model for stiffness. The following equations will characterize the linear regression models,

$$\begin{cases} T_{meas} = K_1\theta_{wg} + T_{st}|\dot{\theta}_{wg}|^\alpha \text{sign}(\dot{\theta}_{wg}) \\ T_{meas} = K_1\theta_{wg} + K_3\theta_{wg}^3 + T_{st}|\dot{\theta}_{wg}|^\alpha \text{sign}(\dot{\theta}_{wg}) \end{cases} \quad (77)$$

Table 6 gives the least square results for cubic stiffness for different experiments. Comparing this results to those in Table 4 for  $\alpha = \frac{1}{2}$ , it is evident that there are more deviations for cubic coefficient of stiffness. The ratio of standard deviation to the average shows a deviation more than 100 %, which is not acceptable. This deviation implies that a cubic model cannot accurately characterize the stiffness in the harmonic drive. To strengthen this conclusion, Figure 33 illustrates the behaviour of nominal model extracted from the average values of Table 6, comparing to the real experiment

$\alpha = 0.5$			
<i>File</i>	$K_1$	$K_3$	$T_{st}$
100-8	$5.0531 \times 10^3$	$6.8074 \times 10^7$	85.910
50-8	$6.0154 \times 10^3$	$3.1314 \times 10^9$	35.352
50-1	$5.8859 \times 10^3$	$7.3199 \times 10^8$	45.898
50-7	$5.677 \times 10^3$	$4.8125 \times 10^8$	60.997
Avg	$5.66 \times 10^3$	$1.10 \times 10^9$	57.0
Std/Avg	6.5%	109%	33.3%

TABLE 6. *Least square results of linear regression model of harmonic drive compliance with cubic stiffness*

hysteresis loop. For high deformation experiments the cubic model estimates much higher torques than what is observed in experiments, and therefore, linear model for stiffness is preferable.

To conclude this section we bring the final form of harmonic drive stiffness and structural damping model.

$$T_{meas} = K_1 \theta_{wg} + T_{st} |\dot{\theta}_{wg}|^\alpha \text{sign}(\dot{\theta}_{wg}) \quad (78)$$

where

$$\begin{cases} K_1 &= 6.34 \times 10^3 \\ T_{st} &= 5.72 \times 10^1 \\ \alpha &= 0.5 \end{cases} \quad (79)$$

Figures 34 and 35 give qualitative comparison of this model for different experiments. Since the average result of different experiments are used as the nominal value, the curve fittings are not perfect for all experiments, but there is acceptable match for different experiments.

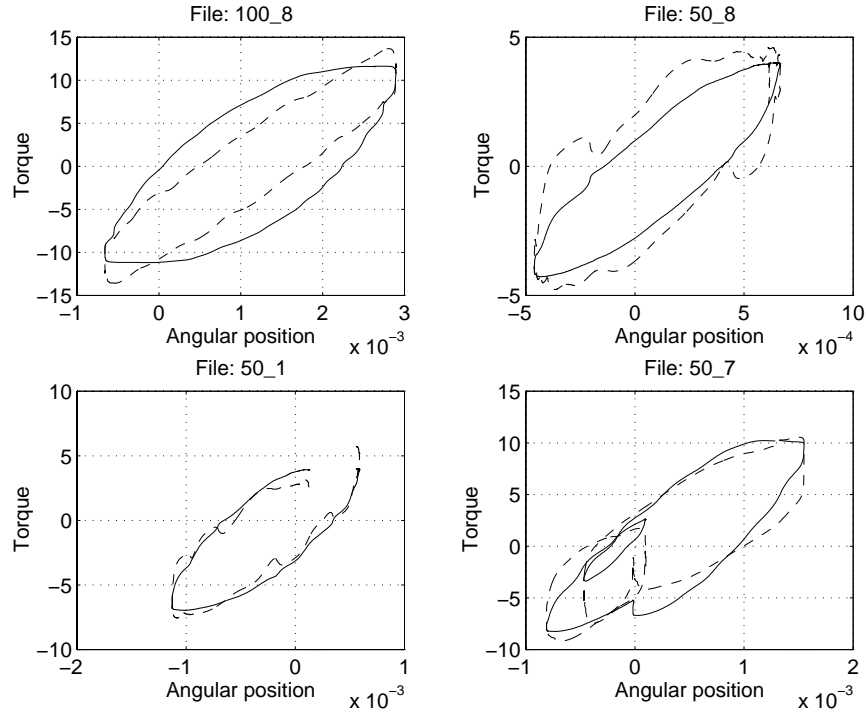


FIGURE 34. Comparison of the experimented hysteresis loop with nominal result of linear stiffness model

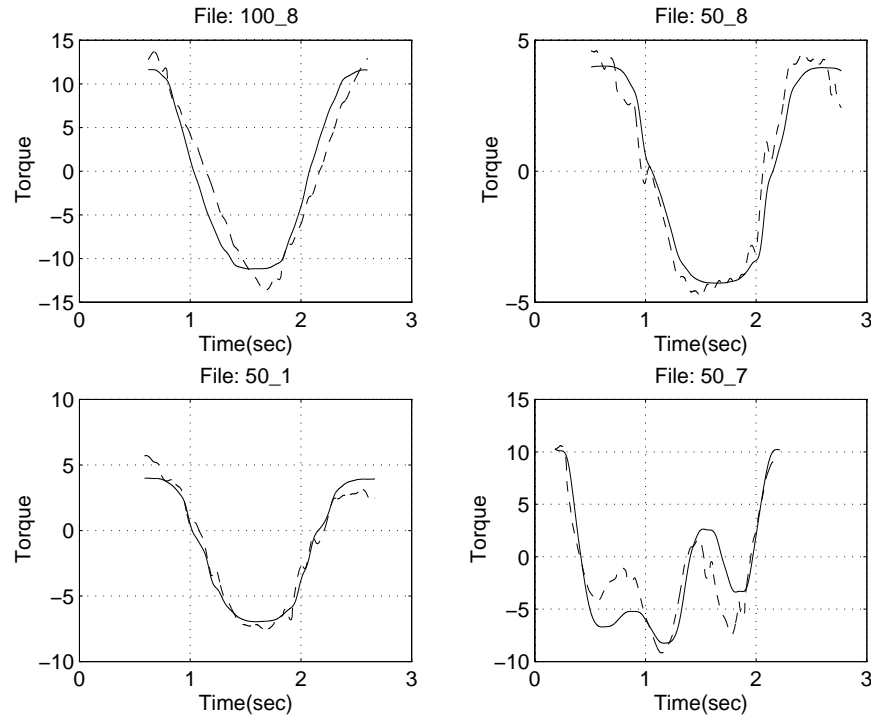


FIGURE 35. Comparison of the experimented torque curve with nominal result of linear stiffness model

### 4.3. Harmonic Drive Friction.

On the contrary to the compliance identification of harmonic drive, to have a persistently exciting experiment for friction, free load experiments is candidated. This is because in the locked load experiments the system is operating in very low speeds, and in this region the velocity dependent friction are not excited. But in free load experiments we can have different speed regions and excite all components of friction. The other benefit of free load experiments is that the output end of the system will move and their parameters can be identified as well. In free load experiments the measured quantities needed for identification are, the motor speed  $\dot{\theta}_{wg}$ , the servo amplifier current  $i$ , the transmitted torque  $T_{meas}$ , and the load angular position  $\theta_{fs}$ , or velocity  $\dot{\theta}_{fs}$ . The first three measurement are the same as that for the locked load experiment, and only the last measurement is added in order to identify the load end parameters. Since the load is operating at low speed, an accurate angular position measurement can be obtained by a digital encoder. This type of measurement has this advantage that it gives an accurate and noise free reading of the output angular position  $\theta_{fs}$ , but it has this disadvantage that direct differentiation from the signal gives a very poor estimate of velocity and acceleration, since the encoder data are quantized. It is noticeable that the accuracy of this differentiation gets even worse by decreasing the sampling time. Since this problem is well known by control practitioners, some solution is given for that. In our group, a good amount of research has been done on this subject, where a Kalman filter estimation is proposed to estimate the angular velocity, and acceleration from encoder readings. Since the details of this is out of scope of this report, the interested reader can refer to Belanger [4], for further background Dobrovolny [10] for detail of implementation, and Canet [7] for on line implementation.

According to Figure 36, and friction model of harmonic drive explained in Section 2.2.3, Equations 41 to 44 can be rewritten in the form of:

$$T_{wg} = T_{f1} + T_{f2} + \frac{1}{N} T_{nfs} \quad (80)$$

where  $T_{wg}$  is the torque transmitted through the wave generator and is equal to:

$$T_{wg} = K_m i - J_{eff} \ddot{\theta}_{wg} - T_{fm} \quad (81)$$

in which  $K_m$ ,  $i$ ,  $J_{eff}$ ,  $T_{fm}$  are servo amplifier torque constant, servo current, total input inertia, and motor friction torque respectively. In DC motor identification,  $K_m$  and

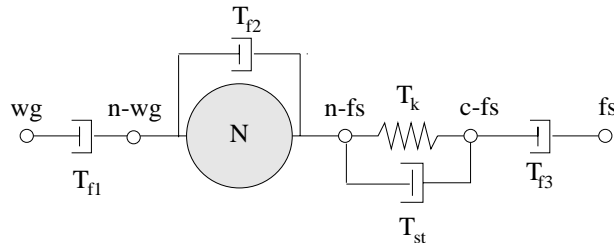


FIGURE 36. *Transmission model of harmonic drive with compliance and friction*

$T_{f_m}$  are already identified, also  $J_m$  is identified but  $J_{eff}$  is the summation of motor inertia and coupling and wave generator inertia is unknown. The final equation which will be used for identification can be written as:

$$K_m i - \frac{1}{N} T_{n_{fs}} = J_{eff} \ddot{\theta}_{wg} + (T_{f_m} + T_{f_1} + T_{f_2}) \quad (82)$$

where  $T_{n_{fs}} = T_{meas}$ , and the left hand side is known by the measurement and previous knowledge of system. The right hand side can be written in form of a parametric equation and form a regression model. It should be mentioned that the friction parameters of the system can not identified separately but rather the whole friction  $T_f = (T_{f_m} + T_{f_1} + T_{f_2})$  will be identified. This cause no major problem since the objective of system identification is for simulation and control and in both case the individual components of friction don't show up. In case of requiring a separate block for motor, the motor friction parameters identified in Section 3.6 can be used and in harmonic drive block we will use the subtraction of DC motor friction parameters from that of the total friction.

#### 4.3.1. Regression Models.

Concluding from the DC motor identification, velocity direction dependent friction is used for harmonic drive friction as well. Also first a linear regression model will provide the high velocity dependent friction parameters, and considering them as known in low velocity experiment the detail Stribeck friction parameters will be identified next using linear or nonlinear regression. So first consider the linear regression model for high velocity experiments. Equation 82 can be rewritten using friction model as:

$$\begin{aligned} K_m i - \frac{1}{N} T_{n_{fs}} = & J_{eff} \ddot{\theta}_{wg} + T_{v_p} \dot{\theta}_{wg} u_{-1}(\dot{\theta}_{wg}) + T_{v_n} \dot{\theta}_{wg} u_{-1}(-\dot{\theta}_{wg}) + \\ & T_{s_p} \text{sign}(\dot{\theta}_{wg}) u_{-1}(\dot{\theta}_{wg}) + T_{s_n} \text{sign}(\dot{\theta}_{wg}) u_{-1}(-\dot{\theta}_{wg}) \end{aligned} \quad (83)$$

where  $u_{-1}(x)$  is the unit step function defined in Equation 28, and the estimation parameter  $\theta$  will be,

$$\theta = [ J_{eff} \quad T_{v_p} \quad T_{v_n} \quad T_{s_p} \quad T_{s_n} ]^T \quad (84)$$

For the low velocity experiments, the abovementioned parameter supposed to be known, and the Stribeck friction parameters can be identified using the following nonlinear regression,

$$\begin{aligned} f(\theta) = & \frac{1}{N} T_{n_{fs}} - K_m i - J_{eff} \ddot{\theta}_{wg} + T_{v_p} \dot{\theta}_{wg} u_{-1}(\dot{\theta}_{wg}) + T_{v_n} \dot{\theta}_{wg} u_{-1}(-\dot{\theta}_{wg}) + \\ & T_{s_p} \text{sign}(\dot{\theta}_{wg}) u_{-1}(\dot{\theta}_{wg}) + T_{s_n} \text{sign}(\dot{\theta}_{wg}) u_{-1}(-\dot{\theta}_{wg}) + \\ & T_{ss_{p1}} \text{sign}(\dot{\theta}_{wg}) u_{-1}(\dot{\theta}_{wg}) e^{-\left(\frac{\dot{\theta}}{T_{ss_{p2}}}\right)^2} + T_{ss_{n1}} \text{sign}(\dot{\theta}_{wg}) u_{-1}(-\dot{\theta}_{wg}) e^{-\left(\frac{\dot{\theta}}{T_{ss_{n2}}}\right)^2} \end{aligned} \quad (85)$$

where in this case the estimation parameters  $\theta$  will be,

$$\theta = [ T_{ss_{p1}} \quad T_{ss_{n1}} \quad T_{ss_{p2}} \quad T_{ss_{n2}} ]^T \quad (86)$$

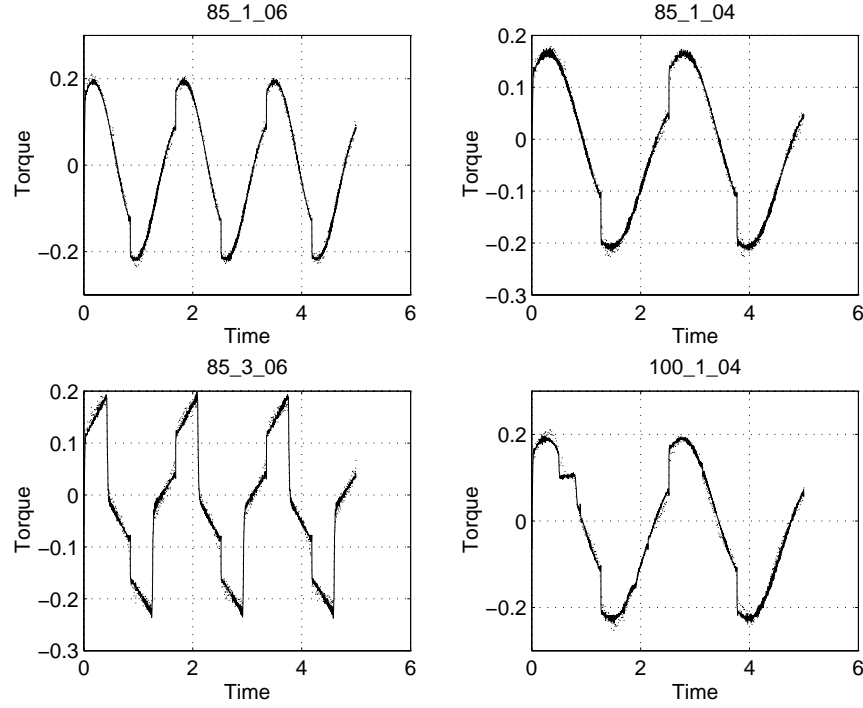


FIGURE 37. Comparison of the least square estimated torque to experiment for four different inputs; dotted: experiment, solid: estimated

In case of fixed  $T_{ss_{p2}}$  and  $T_{ss_{n2}}$  the above nonlinear regression will simplify to a linear regression with only  $T_{ss_{p1}}$  and  $T_{ss_{n1}}$  as estimation parameters. Both nonlinear and linear regression model will be examined through identification process.

#### 4.3.2. Experimental Results.

The experiments are divided into two parts, high speed and low speed experiments. In high speed experiments we used the velocity mode of the servo amplifier, in which the command signal will be tracked as the desired velocity of the DC motor. While, using acceleration mode in low speed experiments where the command signal will be tracked using current feedback of the servo. In both cases different experiment is considered with different frequencies (0.2 - 1 Hz), amplitude (50% -100%) and wave forms. The identification process for high- and low-velocity terms of friction will be discussed in the next sections.

#### High speed friction terms

As explained in DC-motor identification Section 3.7, first a linear regression will be forwarded to estimate the high velocity terms of friction and then using these values, a nonlinear regression will give a better result for the low velocity terms. Equation 84 will be the linear regression model used for the least square solution. Table 7 summarizes the least square results for different experiments. For all of these experiments a very good match exists between the estimated model and the experiment results. Figure 37 illustrates the matching for some of the input signals.

To get a set of nominal values for the model parameters average value of all of trials can be used, which are given in Table 7 as well. Also the ratio of standard deviation to the average value give a better estimate of the deviation in estimation of each parameters. The amount of this value varies for different estimated parameters, but remains smaller than 30% which is the acceptable threshold.

To illustrate how close is our nominal model to experiments, the estimated torque is plotted against the measured torque for different experiments. Figures 38 and 39 give this comparison for different inputs, where a very close match is found in all the experiments.

<i>File</i>	$J_{eff}$	$T_{v_p}$	$T_{v_n}$	$T_{s_p}$	$T_{s_n}$
50-1-02	$1.18 \times 10^{-4}$	$4.60 \times 10^{-4}$	$4.64 \times 10^{-4}$	$4.44 \times 10^{-2}$	$4.82 \times 10^{-2}$
50-1-04	$1.11 \times 10^{-4}$	$4.47 \times 10^{-4}$	$4.44 \times 10^{-4}$	$4.24 \times 10^{-2}$	$4.45 \times 10^{-2}$
50-1-06	$1.05 \times 10^{-4}$	$4.80 \times 10^{-4}$	$4.41 \times 10^{-4}$	$4.80 \times 10^{-2}$	$3.90 \times 10^{-2}$
50-1-08	$1.03 \times 10^{-4}$	$4.65 \times 10^{-4}$	$4.47 \times 10^{-4}$	$4.01 \times 10^{-2}$	$3.76 \times 10^{-2}$
50-1-10	$1.01 \times 10^{-4}$	$4.46 \times 10^{-4}$	$4.52 \times 10^{-4}$	$4.60 \times 10^{-2}$	$3.14 \times 10^{-2}$
50-1-12	$1.02 \times 10^{-4}$	$4.63 \times 10^{-4}$	$4.26 \times 10^{-4}$	$3.81 \times 10^{-2}$	$3.46 \times 10^{-2}$
70-1-02	$1.22 \times 10^{-4}$	$3.26 \times 10^{-4}$	$3.06 \times 10^{-4}$	$5.11 \times 10^{-2}$	$5.49 \times 10^{-2}$
70-1-04	$1.10 \times 10^{-4}$	$3.51 \times 10^{-4}$	$3.03 \times 10^{-4}$	$4.77 \times 10^{-2}$	$5.30 \times 10^{-2}$
70-1-06	$1.04 \times 10^{-4}$	$3.42 \times 10^{-4}$	$3.25 \times 10^{-4}$	$5.72 \times 10^{-2}$	$4.63 \times 10^{-2}$
70-1-08	$1.00 \times 10^{-4}$	$3.59 \times 10^{-4}$	$3.34 \times 10^{-4}$	$4.23 \times 10^{-2}$	$4.73 \times 10^{-2}$
85-1-02	$1.14 \times 10^{-4}$	$3.25 \times 10^{-4}$	$2.47 \times 10^{-4}$	$6.68 \times 10^{-2}$	$3.82 \times 10^{-2}$
85-1-03	$1.07 \times 10^{-4}$	$3.10 \times 10^{-4}$	$2.93 \times 10^{-4}$	$4.41 \times 10^{-2}$	$5.25 \times 10^{-2}$
85-1-04	$1.07 \times 10^{-4}$	$2.89 \times 10^{-4}$	$2.66 \times 10^{-4}$	$5.79 \times 10^{-2}$	$6.26 \times 10^{-2}$
85-1-06	$9.89 \times 10^{-5}$	$3.17 \times 10^{-4}$	$3.05 \times 10^{-4}$	$2.79 \times 10^{-2}$	$6.30 \times 10^{-2}$
85-1-08	$1.00 \times 10^{-4}$	$3.61 \times 10^{-4}$	$3.37 \times 10^{-4}$	$5.61 \times 10^{-2}$	$2.31 \times 10^{-2}$
85-4-04	$9.87 \times 10^{-5}$	$3.12 \times 10^{-4}$	$2.90 \times 10^{-4}$	$4.14 \times 10^{-2}$	$5.80 \times 10^{-2}$
100-1-02	$1.07 \times 10^{-4}$	$3.21 \times 10^{-4}$	$2.66 \times 10^{-4}$	$5.37 \times 10^{-2}$	$4.63 \times 10^{-2}$
100-1-03	$1.04 \times 10^{-4}$	$2.78 \times 10^{-4}$	$2.93 \times 10^{-4}$	$6.19 \times 10^{-2}$	$3.85 \times 10^{-2}$
100-1-04	$1.01 \times 10^{-4}$	$2.98 \times 10^{-4}$	$2.92 \times 10^{-4}$	$6.36 \times 10^{-2}$	$3.49 \times 10^{-2}$
100-1-06	$9.85 \times 10^{-5}$	$3.37 \times 10^{-4}$	$2.90 \times 10^{-4}$	$4.44 \times 10^{-2}$	$4.84 \times 10^{-2}$
50-3-02	$9.35 \times 10^{-5}$	$4.16 \times 10^{-4}$	$3.98 \times 10^{-4}$	$4.02 \times 10^{-2}$	$3.72 \times 10^{-2}$
50-3-04	$9.85 \times 10^{-5}$	$4.05 \times 10^{-4}$	$4.17 \times 10^{-4}$	$3.28 \times 10^{-2}$	$4.21 \times 10^{-2}$
50-3-06	$9.83 \times 10^{-5}$	$4.15 \times 10^{-4}$	$3.85 \times 10^{-4}$	$5.48 \times 10^{-2}$	$2.27 \times 10^{-2}$
50-3-08	$1.02 \times 10^{-4}$	$4.13 \times 10^{-4}$	$3.98 \times 10^{-4}$	$3.76 \times 10^{-2}$	$4.04 \times 10^{-2}$
50-7-02	$1.01 \times 10^{-4}$	$4.02 \times 10^{-4}$	$3.64 \times 10^{-4}$	$2.51 \times 10^{-2}$	$5.36 \times 10^{-2}$
50-7-03	$1.00 \times 10^{-4}$	$3.49 \times 10^{-4}$	$3.77 \times 10^{-4}$	$3.05 \times 10^{-2}$	$5.45 \times 10^{-2}$
Avg	$1.04 \times 10^{-4}$	$3.73 \times 10^{-4}$	$3.52 \times 10^{-4}$	$4.60 \times 10^{-2}$	$4.43 \times 10^{-2}$
Avg/Std	6.38%	16.66%	19.26%	23.69%	24.01%

TABLE 7. *Least square results of linear regression model for high speed friction terms*

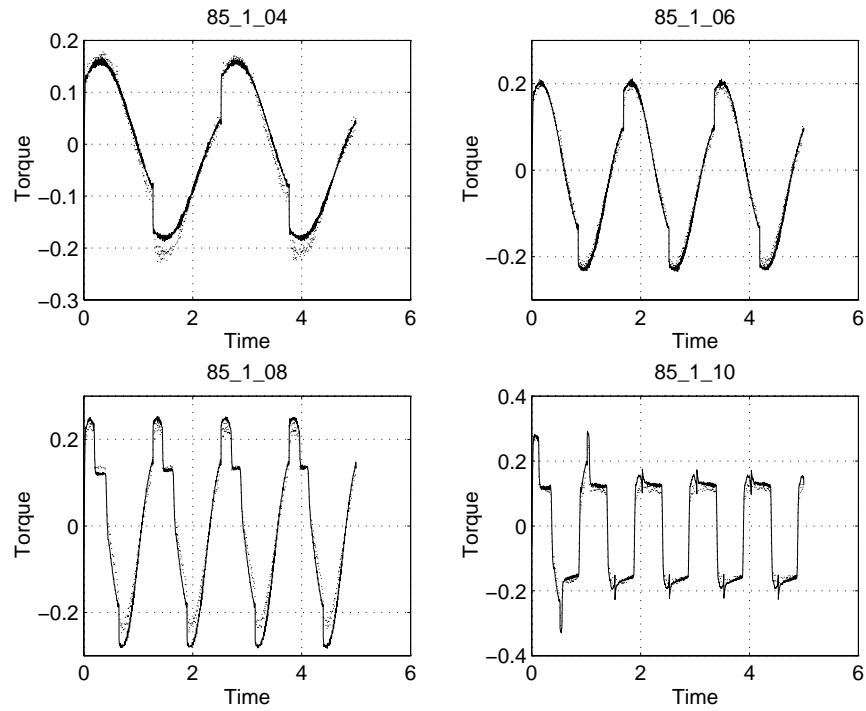


FIGURE 38. Comparison of nominal model torque to experiments for sinusoid inputs; dotted: experiment, solid: estimated

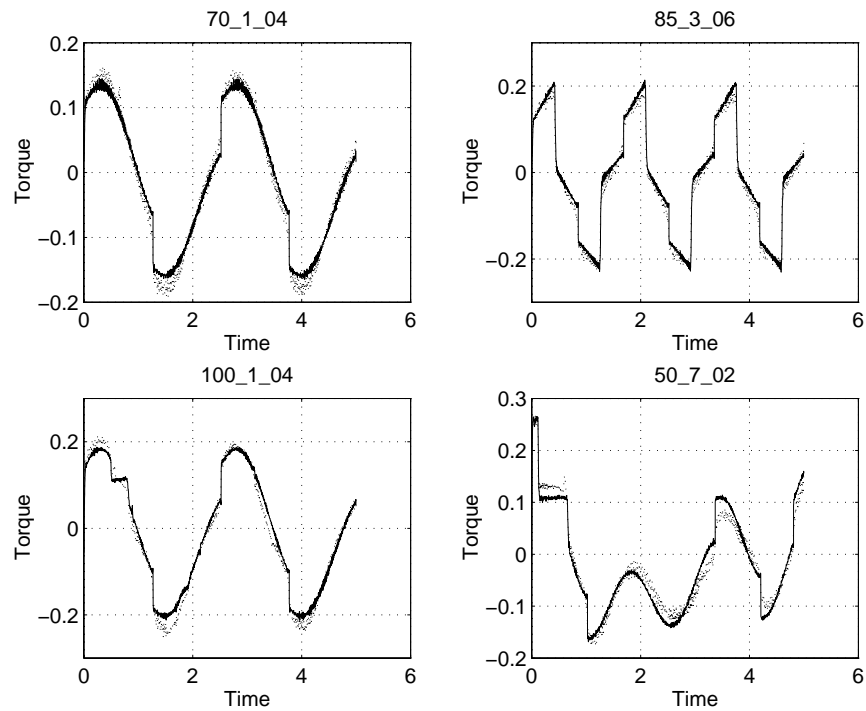


FIGURE 39. Comparison of nominal model torque to experiments for other types of inputs; dotted: experiment, solid: estimated



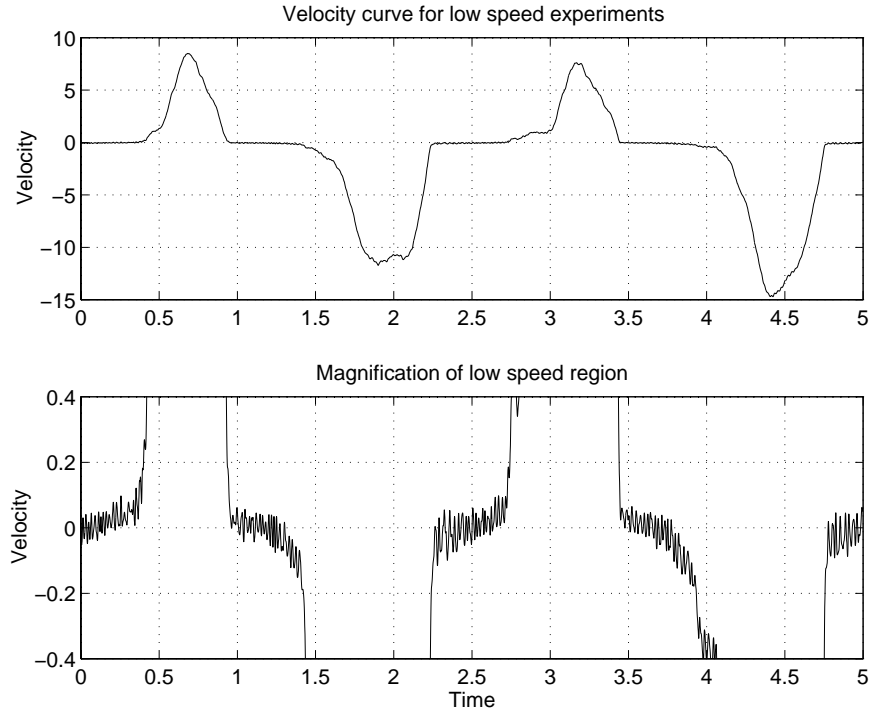
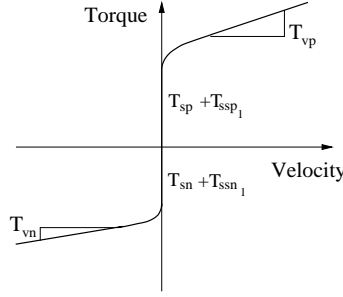


FIGURE 40. *Low velocity experiment: indication of break out in velocity curve*

#### Low speed friction terms

High velocity experiments are not ideal for low velocity regime of friction model. To have a persistently exciting experiment for this region it is required to observe break-up points in the velocity curves. This can be observed using low amplitude triangular input current to the system. Figure 40 illustrates the break-up point in the velocity curve of a typical experiment in which the low velocity region, where we expect a dynamic friction behavior, is approximately between  $\pm 0.1 \text{ rad/s}$ . Fifteen different experiments is done with different current amplitude (18% - 25%), and frequency (0.2 - 1 Hz) in order to be used for low speed friction identification.

By fixing  $T_{ss_{p2}} = T_{ss_{n2}} = 0.1$  and using the linear regression model given in Equation 86 the estimated friction parameters are obtained and given in Table 8. The obtained results for different experiments are close to each other but they are all negative. The ratio of standard deviation to the average value has less than 25% deviation for different results, which is within the acceptable limits. However, the negative sign of the Stribeck friction coefficient is not consistent with the experimental results reported in the literature [2, 16]. Nevertheless, this represents rising friction at low velocities as illustrated in Figure 41, and no stiction, verifying the manufacturers claim [8]. This may be rationalized by the fact that the main bulk of frictional losses in the harmonic drive systems are due to the gear meshing, but that, contrary to other transmissions, a combination of elastic deformation of the flexspline

FIGURE 41. *Identified friction curve*

and gear teeth engagement contributes to the velocity reduction. Therefore, the low-velocity experiments in the harmonic drive transmission shows smoother start up velocity compared to the other transmissions. This is verified by both constrained and unconstrained motion experiments, where no stick slip or stiction is observed. The reliability of the negative Stribeck coefficient is assessed first by obtaining acceptable variation measure for Stribeck coefficients, and second by getting similar results for the two different harmonic drives. The effect of noise and other uncertainties at low velocity experiments is also reduced to a minimum by carefully filtering the signals with a fifth order Butterworth filter, by zero-phase distortion routine. Figure 42 illustrates the model matching of the estimated torque for low velocities experiments, where there is a fairly good match between the estimated torque and experiments.

<i>File</i>	$T_{ssp1}$	$T_{ssn1}$
18-3-02	$-6.5007 \times 10^{-3}$	$-2.4456 \times 10^{-2}$
18-3-04	$-6.7935 \times 10^{-3}$	$-1.9273 \times 10^{-2}$
18-3-06	$-6.3506 \times 10^{-3}$	$-1.7485 \times 10^{-2}$
18-3-08	$-6.2506 \times 10^{-3}$	$-1.1929 \times 10^{-2}$
18-3-10	$-8.3866 \times 10^{-3}$	$-1.4234 \times 10^{-2}$
20-3-04	$-9.2358 \times 10^{-3}$	$-2.4831 \times 10^{-2}$
20-3-06	$-4.6380 \times 10^{-3}$	$-1.8455 \times 10^{-2}$
20-3-08	$-1.1474 \times 10^{-2}$	$-1.6857 \times 10^{-2}$
20-3-10	$-9.0822 \times 10^{-3}$	$-1.4842 \times 10^{-2}$
22-3-02	$-1.1461 \times 10^{-2}$	$-2.6649 \times 10^{-2}$
22-3-04	$-7.8445 \times 10^{-3}$	$-2.0859 \times 10^{-2}$
22-3-06	$-7.8609 \times 10^{-3}$	$-1.9323 \times 10^{-2}$
25-3-02	$-4.8664 \times 10^{-3}$	$-2.8397 \times 10^{-2}$
25-3-04	$-8.0271 \times 10^{-3}$	$-1.9585 \times 10^{-2}$
25-3-06	$-7.2609 \times 10^{-3}$	$-1.8650 \times 10^{-2}$
Avg	$-7.61 \times 10^{-3}$	$-2.03 \times 10^{-2}$
Std/Avg	14.7%	23.8%

TABLE 8. *Least square results of Stribeck friction coefficients in harmonic drive*

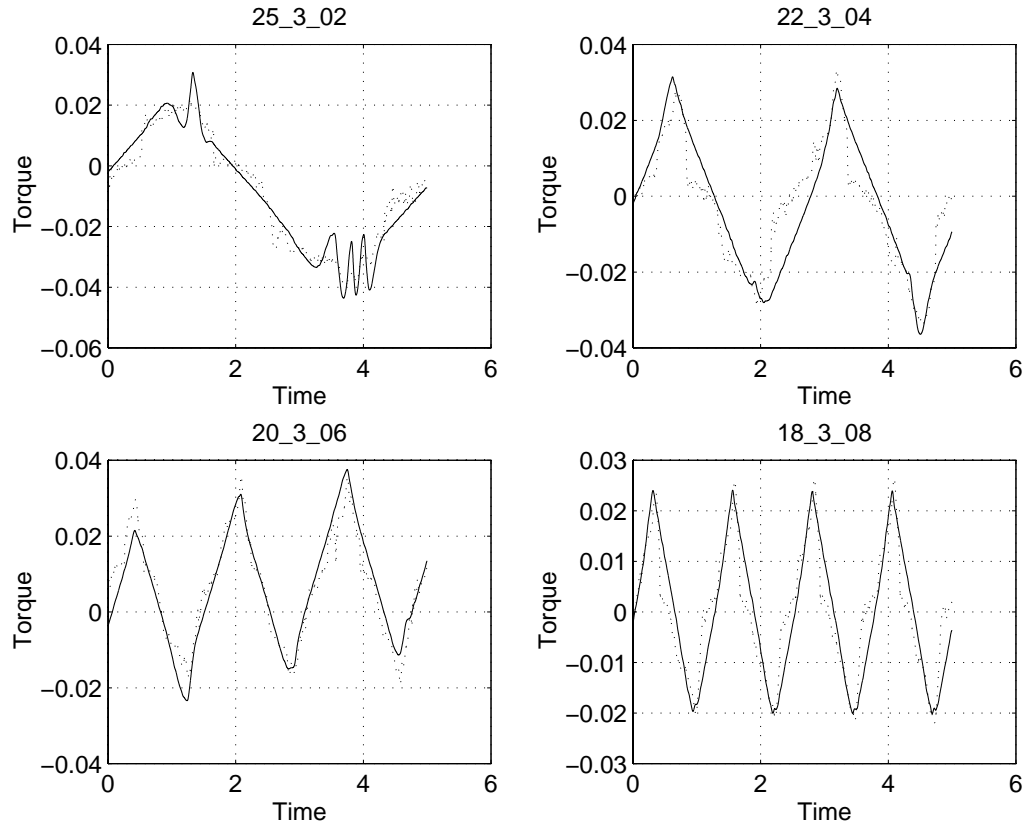


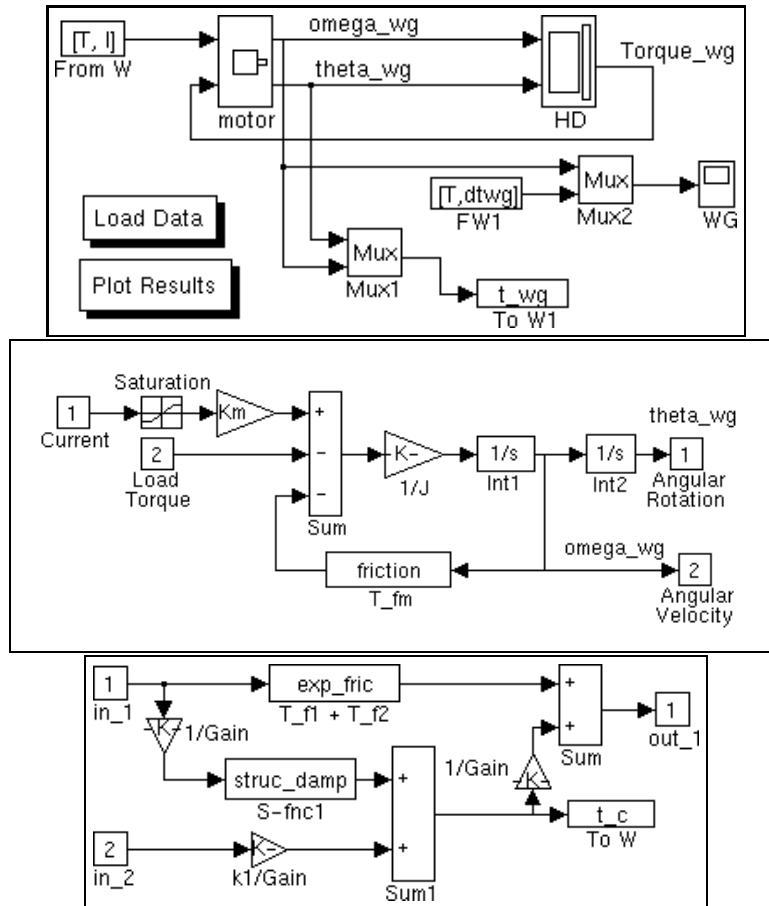
FIGURE 42. *Comparison of nominal model torque to experiments for low speed experiments*

.

## 5. MODELLING AND IDENTIFICATION VERIFICATION

## 5.1. System under Locked-Load Motion.

To verify the validity and integrity of the model, simulations of the system for both locked-load and free motion cases are developed in Simulink. Figure 43 illustrates the block diagram of the locked-load motion simulation, in which the internal simulation blocks of DC motor and harmonic drive are shown separately. To show the model fidelity a framework to compare simulation and experiment result is developed in this simulation, in which the measured motor current in the experiments are used as an input to the simulations, while the simulated torque and velocity of the system can be compared to that of the experiments. Moreover, in order to have a user friendly simulation, it is only required to double click on “Load Data” block in the main simulation module illustrated in Figure 43, to download the model parameters as well as the experimental data. By pressing “Plot Results” block, the



final velocity and torque comparison plots is automatically generated in Matlab environment. A Runge–Kutta fixed–step integration method with  $1\text{ms}$  integration steps is used to execute these simulations, consistent with the  $1\text{ kHz}$  sampling frequency in the experiments. Furthermore, in order to speed up the simulations all internal nonlinear functions (i.g. friction block) are written in C as S–functions in Simulink and compiled using Cmx compiler.

**5.2. System under Free–Motion.** Figure 44 illustrates the simulation module for the system under free motion experiments in which the internal simulation blocks of DC motor and harmonic drive are shown separately. Similar to Figure 43, measured

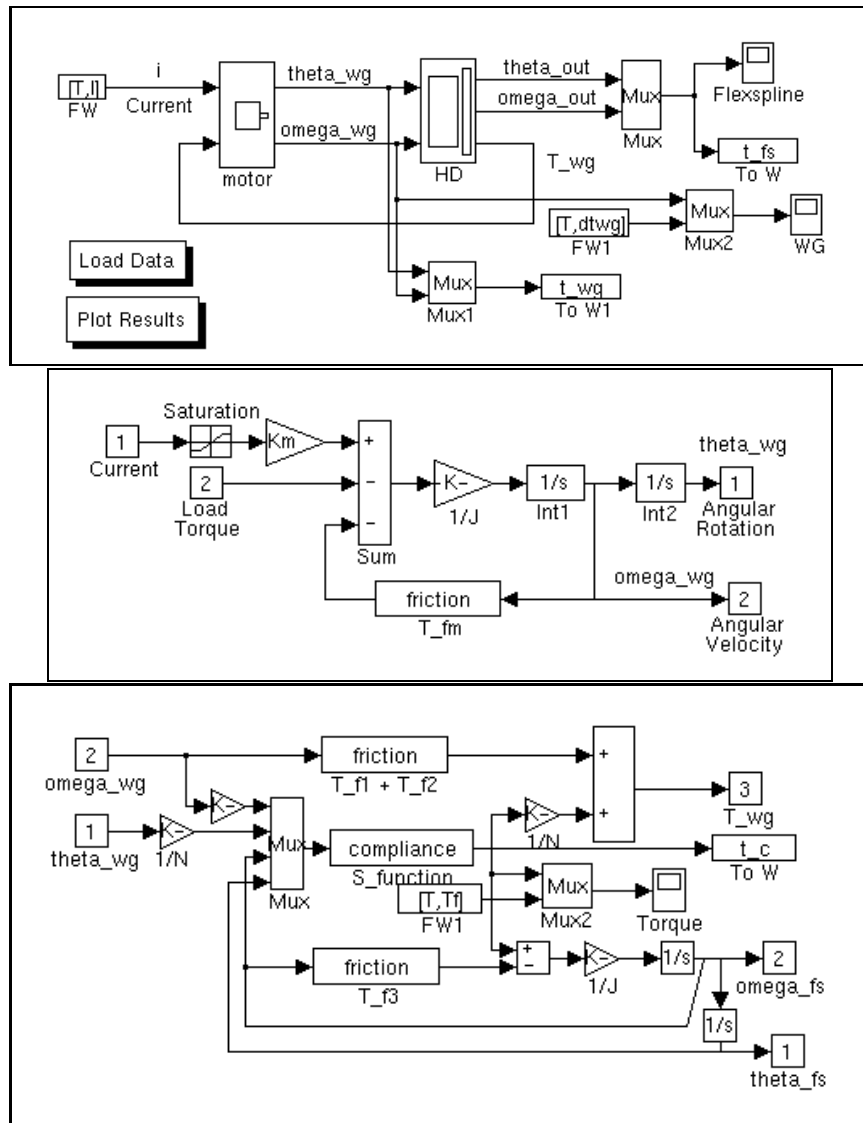


FIGURE 44. System under free motion simulated on Simulink for model verification purpose. Top: System; Mid: DC–motor; Bot: Harmonic drive

current in the experiments are used as an input to the simulations, while the simulated torque and velocity of the system can be compared to that of the experiments. The velocity and torque comparison of system under both locked-load and free motion with experimental results is detailed in Section 5.3.

### 5.3. Comparison of the Simulation and Experiment.

The output velocity and torque of the simulated system are compared to typical experimental outputs in Figure 45. The experimental signals are filtered using a fifth order Butterworth filter, by zero-phase distortion routine. Therefore, the torque ripples in free motion experiments, and the noise on the measured velocity in locked-load motion experiments are not displayed in Figure 45. For the system under free motion, there is an almost perfect match for the velocity, and a relatively good match for torque curves, except for the torque ripples. It should be mentioned that to have an accurate model to predict the torque ripples requires a complex gear meshing mechanism modelling, [29], which is not pursued in this research. However, we have shown in [25], that a Kalman filter estimation of the torque ripples, using simple harmonic oscillator model, can accurately estimate the torque ripples. For the system under locked-load motion, the match between velocities is less accurate compared to that for the free motion system, which is because of the smaller velocity signal and

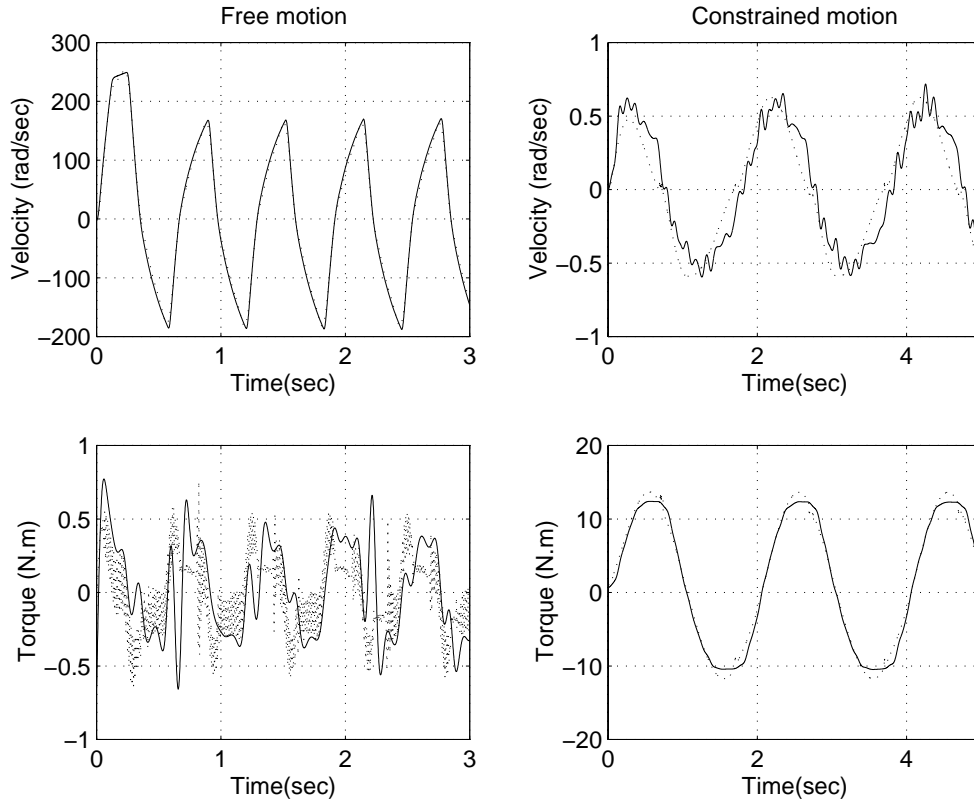


FIGURE 45. Simulation verification for system under free and locked-load motion; Solid : Experiment, Dotted : Simulation

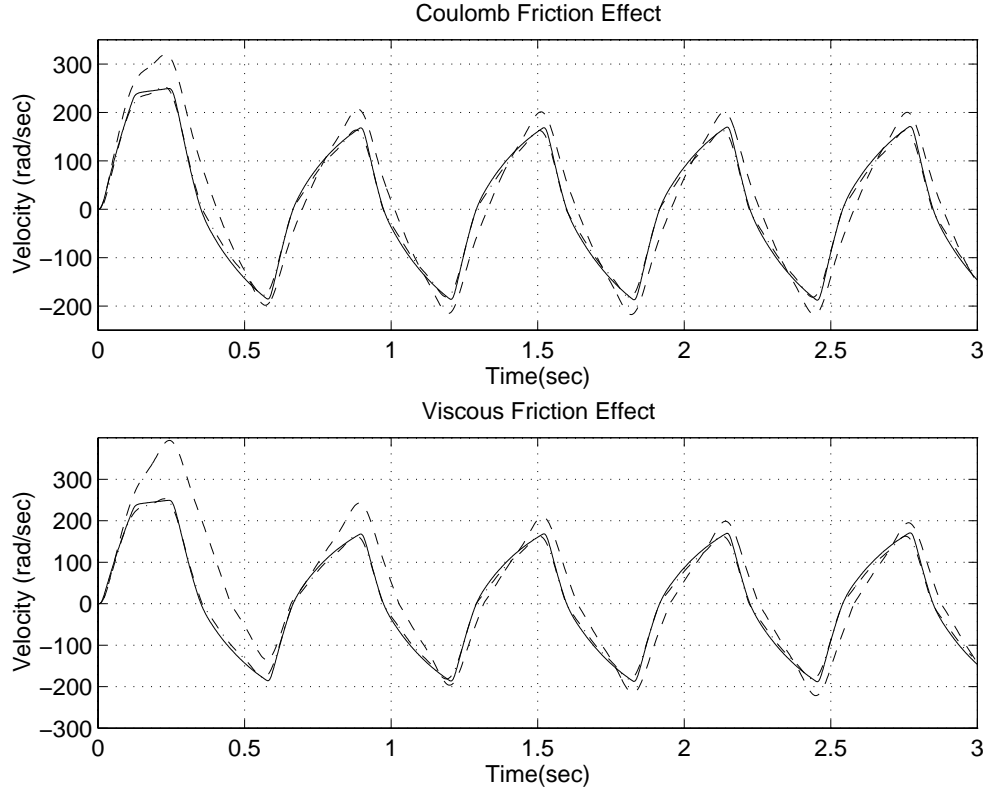


FIGURE 46. Comparison of the experiment with the complete and simplified model, where the significance of Coulomb and viscous friction are examined separately; Solid : Experiment, Dash-dotted : Complete model, Dashed : Simplified model

hence smaller signal-to-noise ratio. However, the resulting torques are quite similar and there is no torque ripple observed for the locked-load system. This accurate match was verified for more than twenty other experiments for the setup, and similar results are obtained for both locked-load and free motion systems, where some of them are illustrated in Appendix A. The accurate match between simulation and experiment for different operating ranges, indicates the fidelity of the model to accurately replicate the dynamic behavior of the system, and confirmed the effectiveness of modelling and parameter identification schemes to capture the dynamics of the harmonic drive systems.

#### 5.4. Parameter Sensitivity Study.

To realize the significance of the nonlinear model and compare it to simpler models, a simulation study is done in which, for a set of experiments, the simulation results of the complete model is compared to that of the simplified model. In this study the importance of Coulomb, viscous, and Stribeck model for friction as well as stiffness and structural damping model has been examined. To examine the effect of Coulomb and viscous friction, the simulation of the system under free motion constructed for model verification is used, which is illustrated in Figure 44. For



Simplified model, either Coulomb or viscous friction coefficient is set to zero and the simulation results are compared to that for complete model, and experiment. Figure 46 illustrates the results of the comparison for a typical experiment, where in absence of either Coulomb friction or viscous friction the model is not capable of accurately estimating the experimental result. Hence, accurate identification of Coulomb and viscous friction coefficients significantly contributes to the accuracy of the simulations. Stribeck friction coefficients, however, are found to contribute only in very low-velocity experiments, and their effect for the typical experiment of Figure 46 is negligible. Hence, in applications where fine motions at low velocities are demanded modelling and identification of Stribeck friction is vital.

The importance of the compliance model to accurately replicate the experiments are assessed using the simulations of system under locked-load motion illustrated in Figure 43. For simplified models first stiffness is reduced by one order of magnitude, and then structural damping coefficient is set to zero, while keeping all the other identified parameters of the model. In this way the effect of stiffness and structural damping can be studied separately. Figure 47 illustrates a typical comparison of the simplified model to the complete model for one experiment. It is observed in

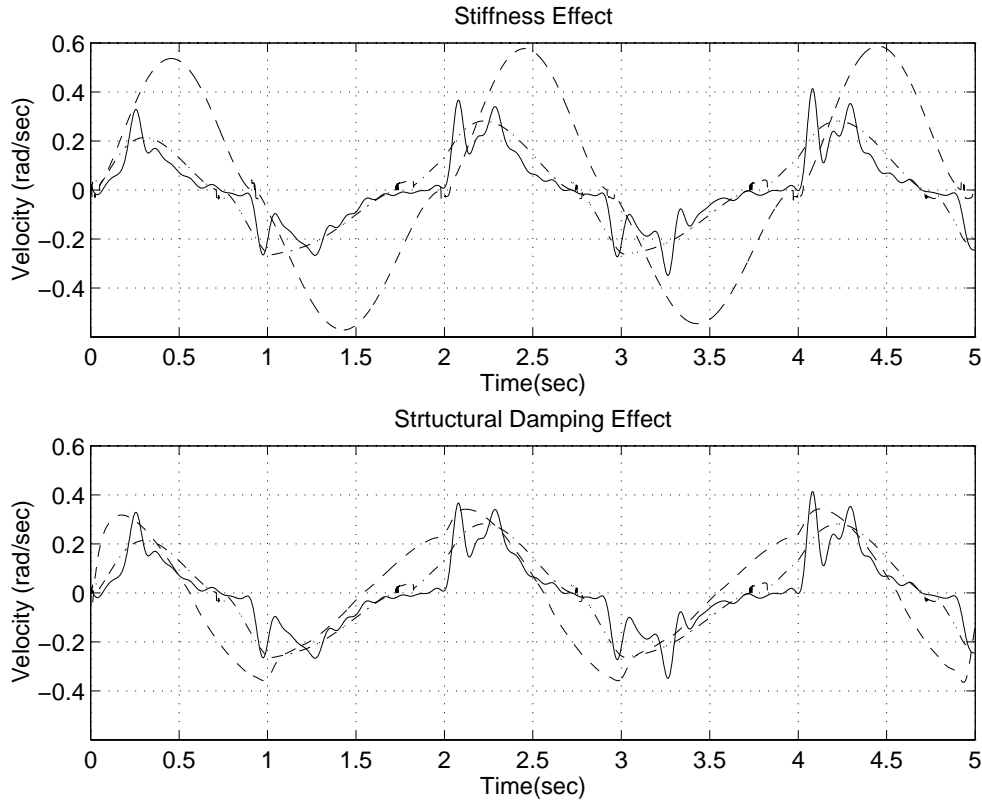


FIGURE 47. Comparison of the experiment with the complete and simplified model, where the significance of stiffness and structural damping are examined separately; Solid : Experiment, Dash-dotted : Complete model, Dashed : Simplified model

Figure 47, that lack of accuracy in identifying the stiffness parameter results in larger velocity amplitude in the simulations. Furthermore, inaccurate structural damping coefficient results in phase estimation of the velocity. Therefore, both stiffness and structural damping coefficients contribute significantly into accuracy of the model.

## 6. CONCLUSIONS

Based on experimental and theoretical studies, a systematic way to capture and rationalize the dynamics of the harmonic drive systems is introduced. Simple and accurate models for compliance, hysteresis, and friction are established and model parameters are identified using least-squares approximation. A measure of variation is defined, by which the reliability of the estimated parameter for different operating condition, as well as the accuracy of the simple model is quantified. From compliance modelling results, it has been shown that identifying stiffness and structural damping together will resolve the reported difficulties in determining the compliance parameters. Moreover, it has been shown that a linear stiffness model best captures the behavior of system when combined with a good model for hysteresis. A simple static model for hysteresis is also introduced, and it is shown that this simple model can replicate the hysteresis effect in harmonic drives better than some other more complex dynamic models reported in the literature. Friction losses of the harmonic drive are modelled at both low and high velocities. From experiments on two different harmonic drives it has been observed that there is no stiction in the transmission, but rather a rising friction acts at low velocities. Finally, the model performance is assessed by a simulation verifying the experimental results for both locked- and free-load systems.

.

## REFERENCES

- [1] B. Armstrong. Stick-slip arising from stribek friction. *Proceeding of IEEE International Conference on Robotics and Automation*, pages 1377–1382, 1990.
- [2] B. Armstrong-Helouvry. Stick slip and control in low speed motion. *IEEE Transactions on Automatic Control*, 38(10):1483–1496, October 1993.
- [3] B. Armstrong-Helouvry, P. Dupont, and C. Canudas de wit. A survey of models, analysis tools and compensation methods for control of machines with friction. *Automatica*, 30(7):1083–1138, 1994.
- [4] P.R. Belanger. Estimation of angular velocity and acceleration from shaft encoder measurements. Technical Report TR-CIM-91-1, Center for Intelligent Machines, 1991.
- [5] J.E. Bernard. The simulation of coulomb friction in mechanical systems. *Simulation*, 34(1):11–16, 1980.
- [6] P.J. Bliman. Mathematical study of dahl’s friction model. *European Journal of Mechanics, A / Solids*, 11(6):835–848, 1992.
- [7] P. Canet. Kalman filter estimation of angular velocity and acceleration: On-line implementation. Technical Report TR-CIM-95-15, Center for Intelligent Machines, November 1994.
- [8] J.H. Charlson. Harmonic drives for servomechanisms. *Machine design*, 57(1):102–106, January 1985.
- [9] P.R. Dahl. Solid friction damping of mechanical vibration. *AIAA Journal*, 14(12):1675–1682, December 1976.
- [10] P. Dobrovolsky. Kalman filter estimation of angular velocity and acceleration. Technical Report TR-CIM-94-4, Center for Intelligent Machines, April 1994.
- [11] P.E. Dupont. Avoiding stick-slip in position and force control through feedback. *Proceeding of IEEE International Conference on Robotics and Automation*, pages 1470–1475, April 1991.
- [12] G.H. Golub and C. Van Loan. *Matrix computations*. The Johns Hopkins University Press, Baltimore, MD, 1983.
- [13] D.A. Haessig and B. Friedland. On the modeling and simulation of friction. *Journal of Dynamic Systems, Measurement and Control*, 113(3):354–362, 1991.
- [14] M. Hashimoto, Y. Kiyosawa, H. Hirabayashi, and R.P. Paul. A joint torque sensing technique for robots with harmonic drives. *Proceeding of IEEE International Conference on Robotics and Automation*, 2:1034–1039, April 1991.
- [15] M. Hashimoto, K. Koreyeda, T. Shimono, H. Tanaka, Y. Kiyosawa, and H. Hirabayashi. Experimental study on torque control using harmonic drive built-in torque sensors. *Proceeding of IEEE International Conference on Robotics and Automation*, pages 2026–2031, May 1992.
- [16] D.P. Hess and A. Soom. Friction at a lubricated line contact operating at oscillating sliding velocities. *Journal of Tribology*, 112(1):147–152, January 1990.
- [17] L. Hsia. The analysis and design of harmonic gear drives. *Proceedings of the 1988 IEEE International Conference on Systems, Man and Cybernetics*, 1:616–619, 1988.
- [18] N. Kircanski, A. Goldenberg, and S. Jia. An experimental study of nonlinear stiffness, hysteresis, and friction effects in robot joint with harmonic drives and torque sensors. *Proceedings of the Third International Symposium on Experimental Robotics*, 1:147–154, 1993.
- [19] G. Legnani and R. Faglia. Harmonic drive transmission: the effect of their elasticity, clearance and irregularity on the dynamic behaviour of an actual scara robot. *Robotica*, 10:369–375, October 1992.
- [20] J.W. Macki, P. Nistri, and P. Zecca. Mathematical models for hysteresis. *SIAM Review*, 35(1):94–123, March 1993.
- [21] T. Marillier and J.A. Richard. Non-linear mechanic and electric behavior of a robot axis with a harmonic-drive gear. *Robotics and Computer-Integrated Manufacturing*, 5(2/3):129–136, 1989.
- [22] J.A.C. Martins, J.T. Oden, and F.M.F. Simoes. A study of static and kinetic friction. *Int. J. Eng. Sci.*, 28(1):29–92, 1990.

- [23] H.D. Taghirad and P.R. Belanger. An experimental study on modelling and identification of harmonic drive systems. *Proceeding of IEEE Conference on Decision and Control*, 4:4725–30, Dec 1996.
- [24] H.D. Taghirad, P.R. Belanger, and A. Helmy. An experimental study on harmonic drive. *Technical Report Submitted to the International Submarine Engineering Ltd., Port Coquitlam, BC, Canada*, <http://www.cim.mcgill.ca/taghirad> 1996.
- [25] H.D. Taghirad, A. Helmy, and P.R. Belanger. Intelligent built-in torque sensor for harmonic drive system. *To be presented in the 1997 IEEE Instrumentation and Measurement Technology Conference*, May 1997.
- [26] D.C. Threlfall. The inclusion of coulomb friction in mechanisms programs with particular reference to DRAM. *Mech. and Mach. Theory*, 13:475–483, 1978.
- [27] T.D. Tuttle. Understanding and modeling the behavior of a harmonic drive gear transmission. Technical Report 1365, MIT Artificial Intelligence Laboratory, 1992.
- [28] T.D. Tuttle and W. Seering. Modeling a harmonic drive gear transmission. *Proceeding of IEEE International Conference on Robotics and Automation*, 2:624–629, 1993.
- [29] T.D. Tuttle and W.P. Seering. A nonlinear model of a harmonic drive gear transmission. *IEEE Transaction on Robotics and Automation*, 12(3):368–374, June 1996.

## APPENDIX A. SIMULATION VERIFICATION PLOTS

In this appendix some more comparison plots of the simulation and experimental results for the system under constrained and free motion are presented. Experiment with different input shape functions, and frequencies are examined and illustrated. Section 5.3 discusses the fidelity of the model to accurately replicate the dynamic behavior of the system based on Figure 45 which is a typical example of the following figures. In all figures Solid line represents the filtered measured signals from the experiments, while dotted line represents the simulation outputs.

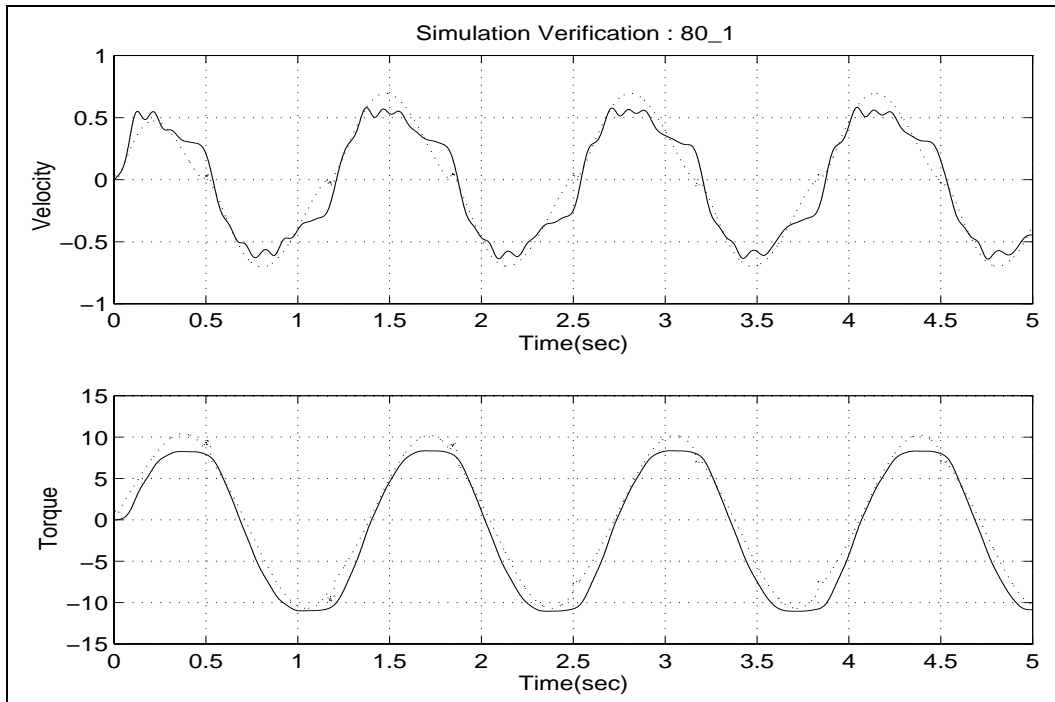


FIGURE 48. Locked-load simulation verification: Sinusoid input, 80% of maximum amplitude.

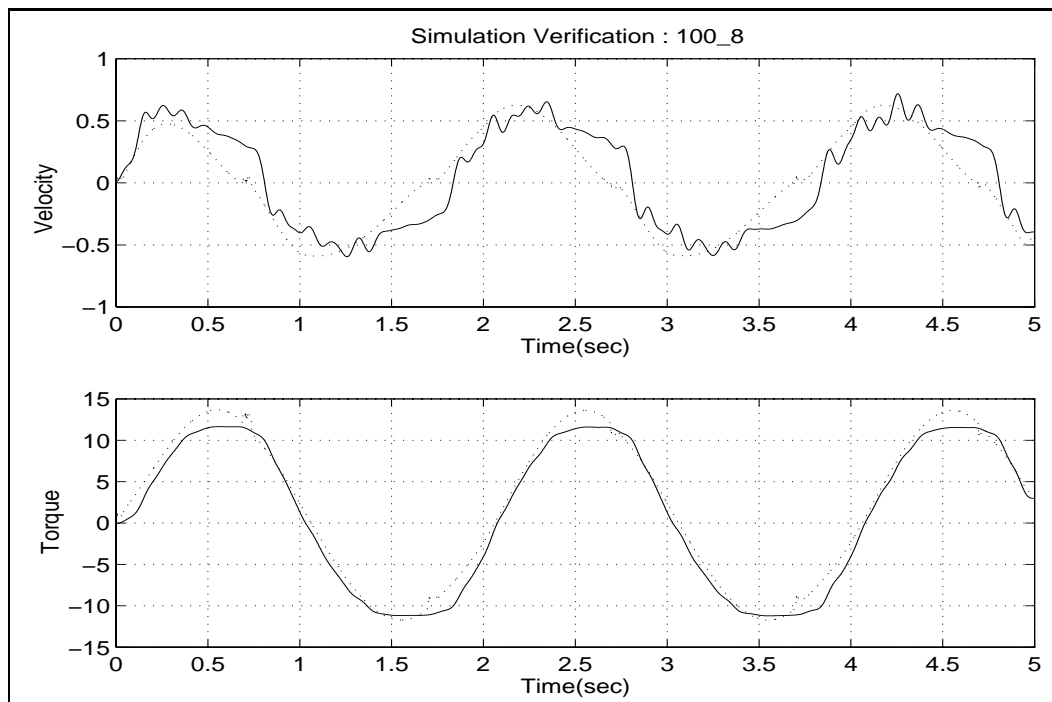


FIGURE 49. Locked-load simulation verification: Asymmetric sinusoid input, with maximum amplitude.

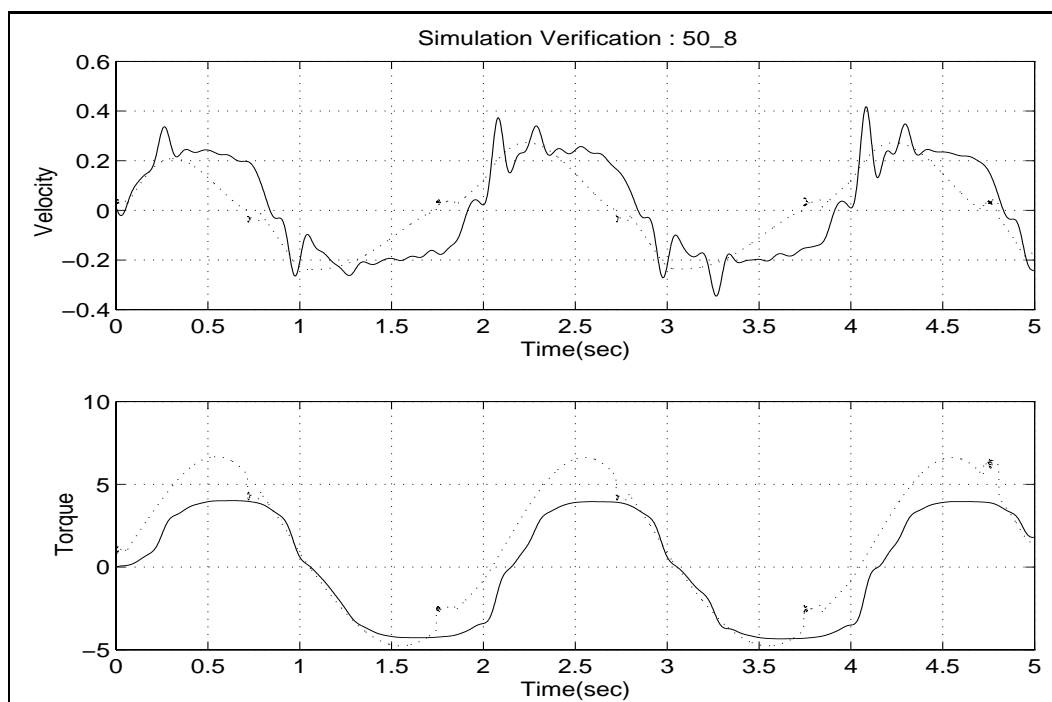


FIGURE 50. Locked-load simulation verification: Asymmetric sinusoid input, 50% of maximum amplitude.



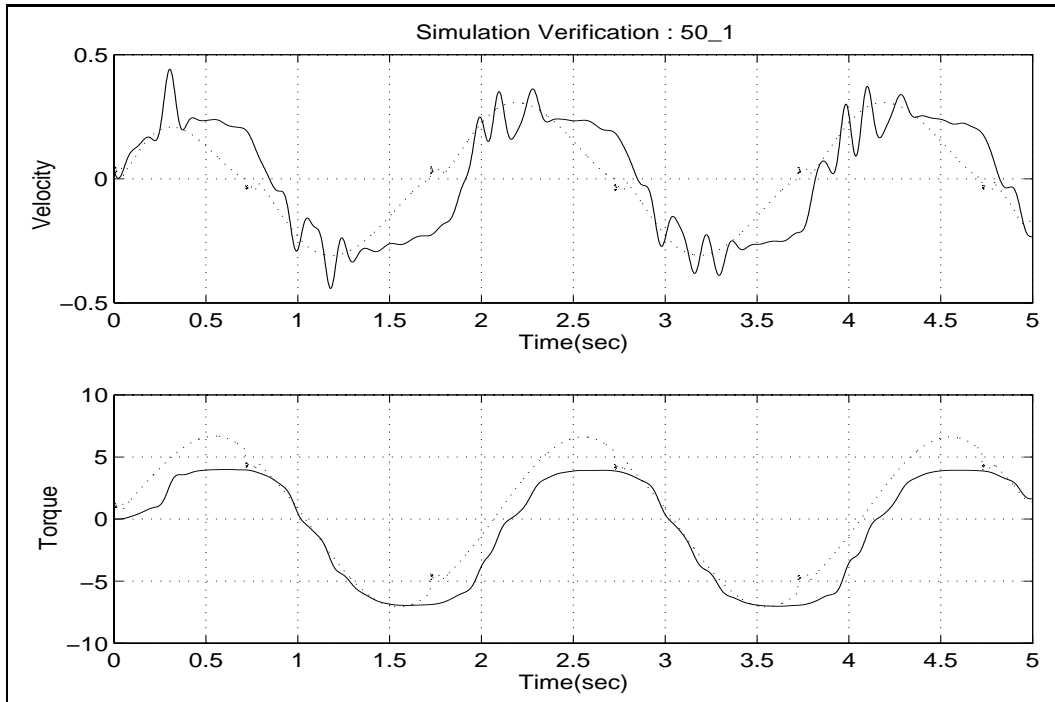


FIGURE 51. Locked-load simulation verification: Sinusoid input, 50% of maximum amplitude.

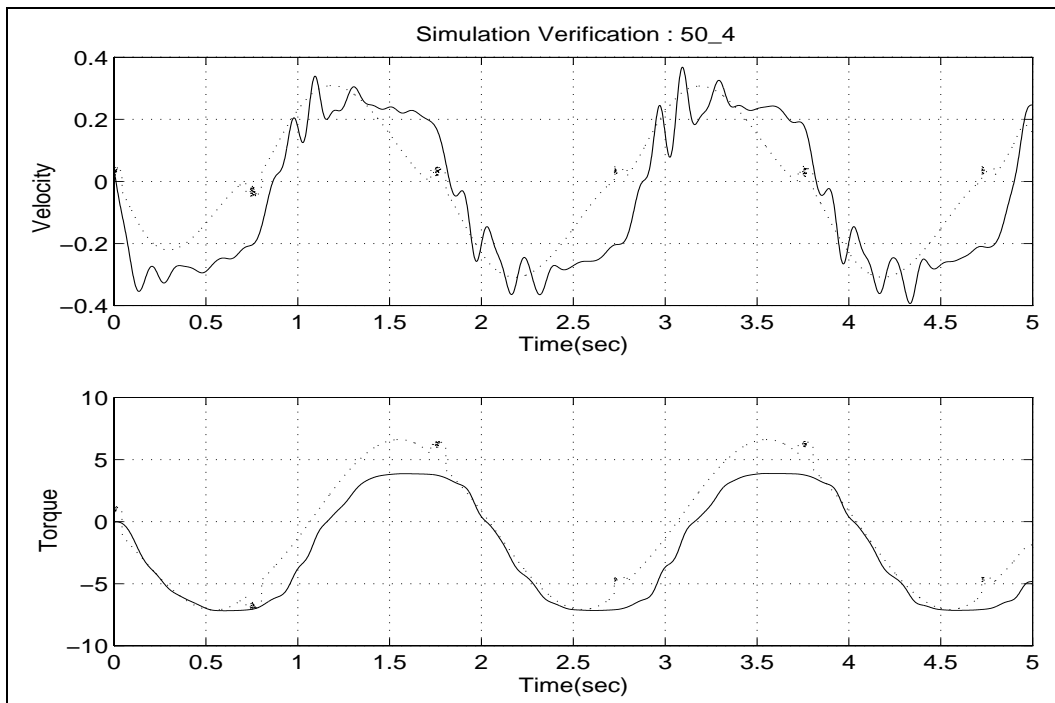


FIGURE 52. Locked-load simulation verification: Inverted sinusoid input, 50% of maximum amplitude.

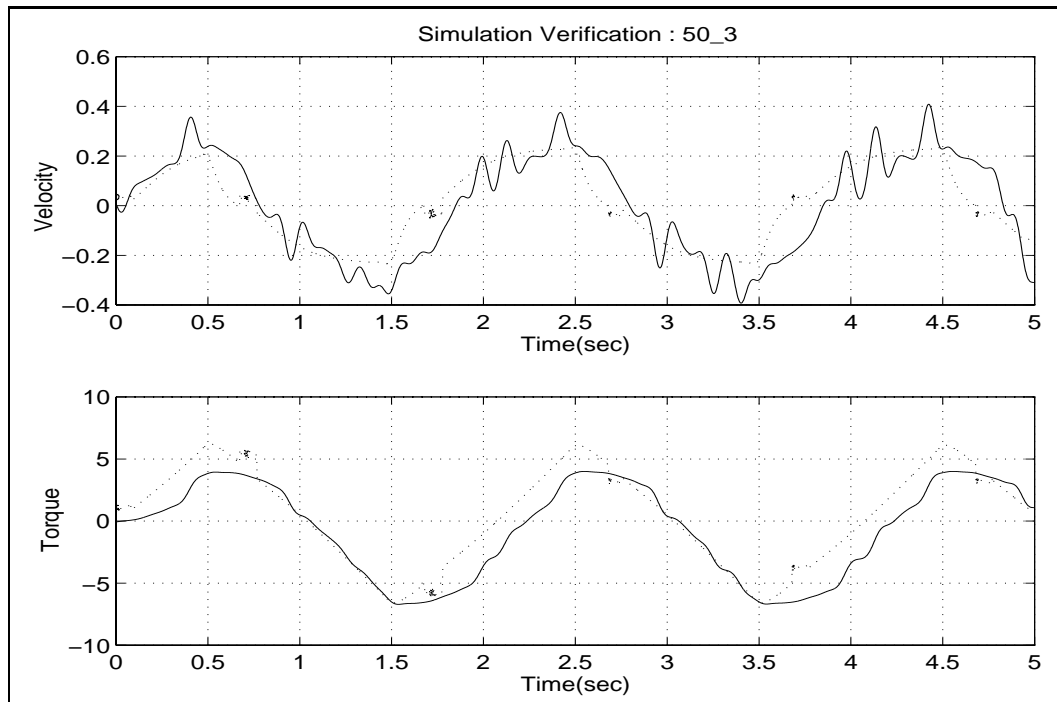


FIGURE 53. Locked-load simulation verification: Trianglur input, 50% of maximum amplitude.

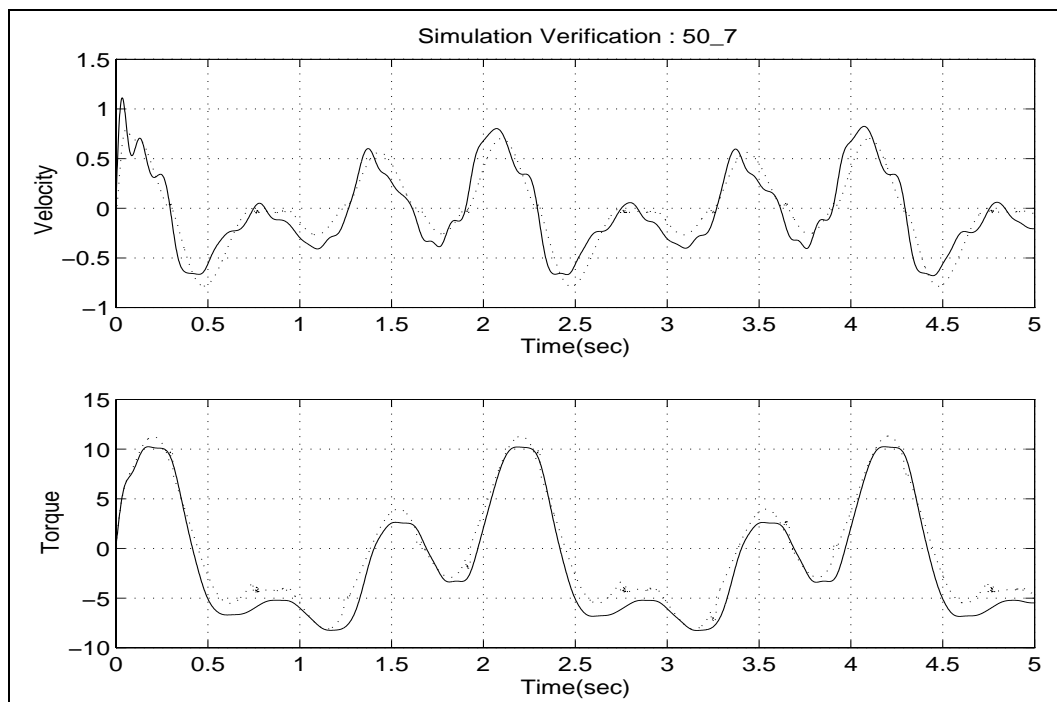


FIGURE 54. Locked-load simulation verification: Composite Sine input, 50% of maximum amplitude.

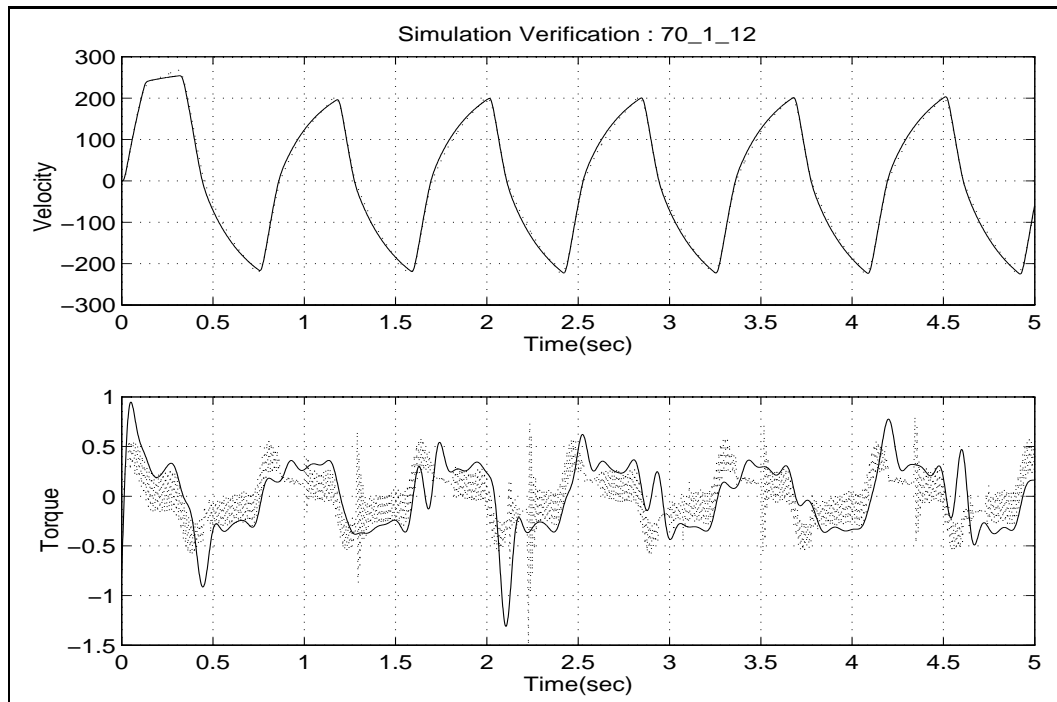


FIGURE 55. Free-motion simulation verification: 1.2 Hz sinusoid input

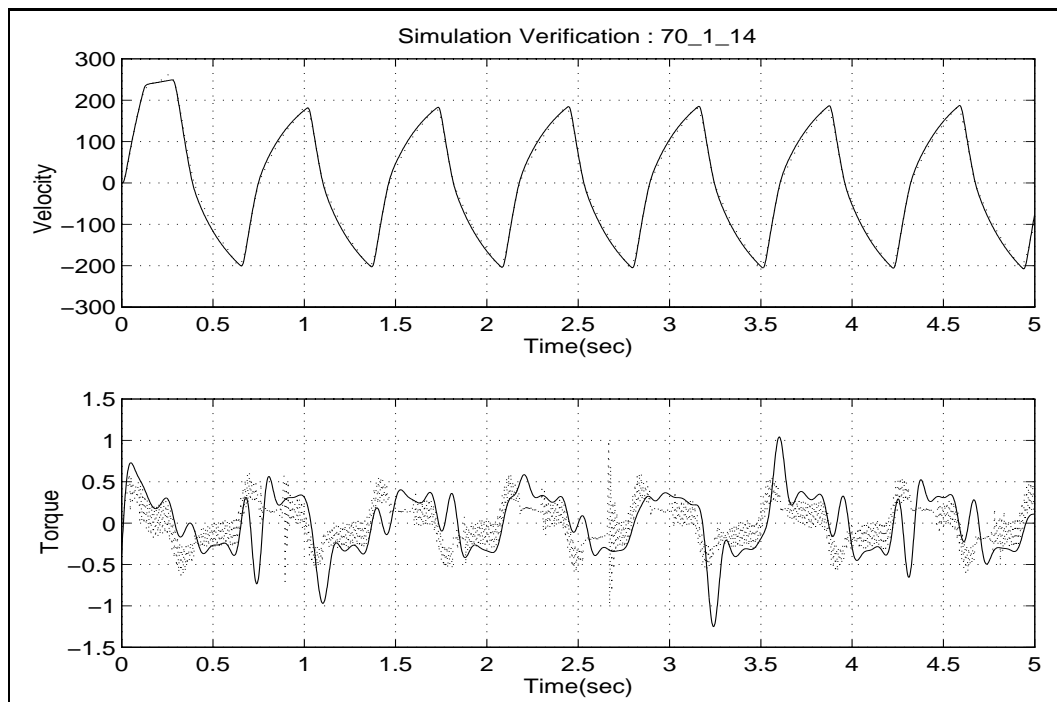


FIGURE 56. Free-motion simulation verification: 1.4 Hz sinusoid input

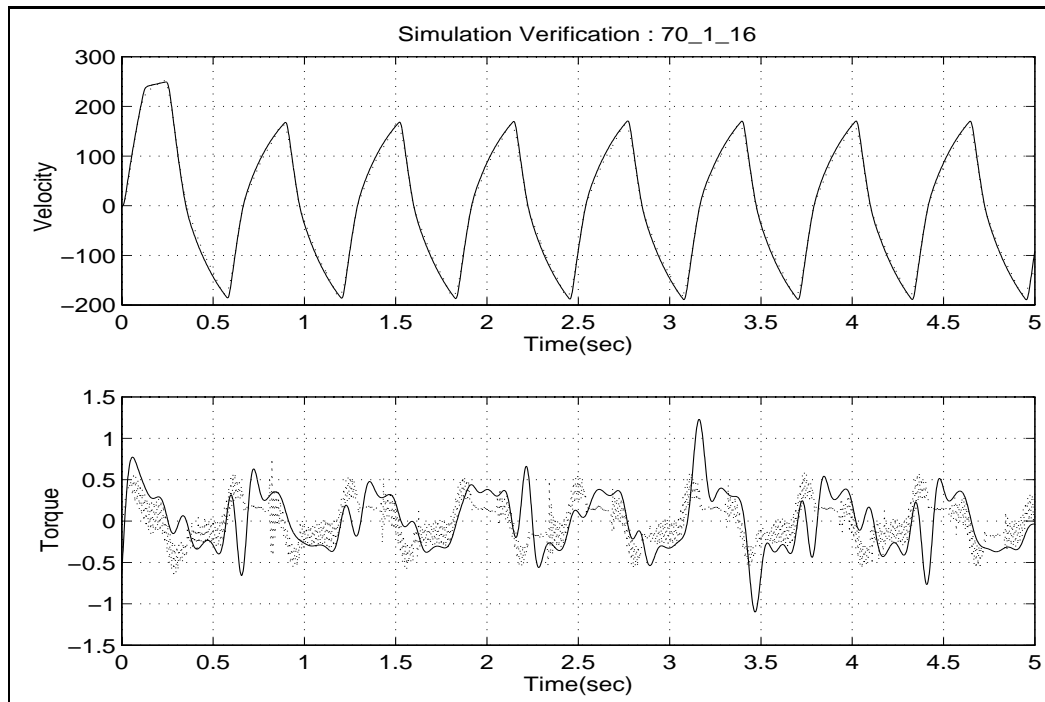


FIGURE 57. Free-motion simulation verification: 1.6 Hz sinusoid input

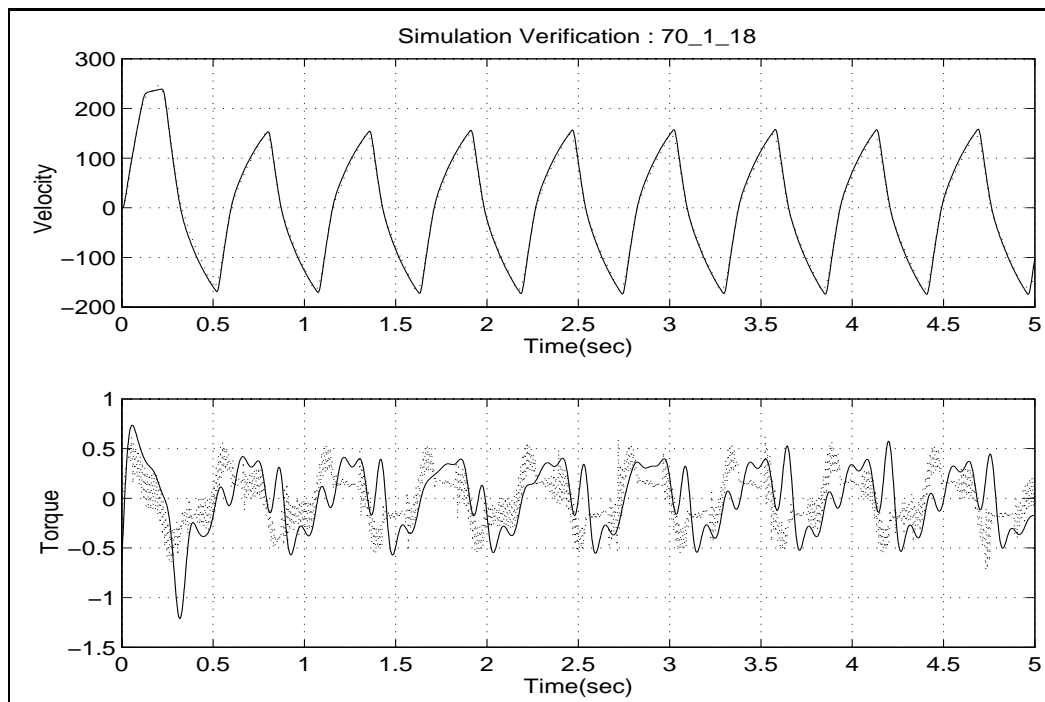


FIGURE 58. Free-motion simulation verification: 1.8 Hz sinusoid input

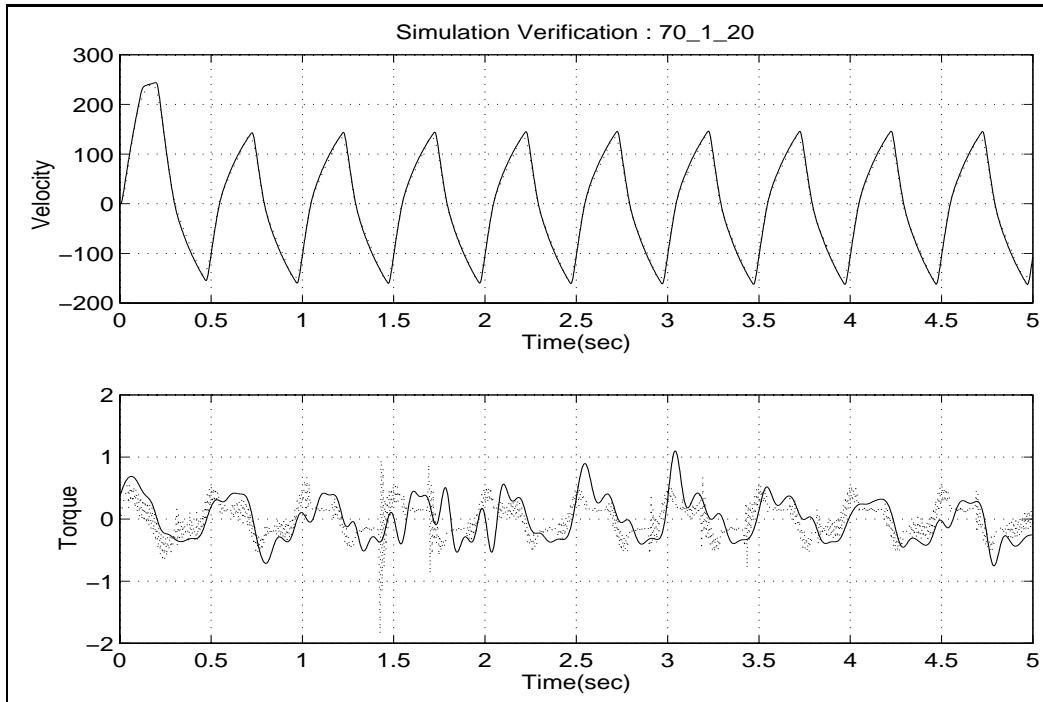


FIGURE 59. Free-motion simulation verification: 2 Hz sinusoid input

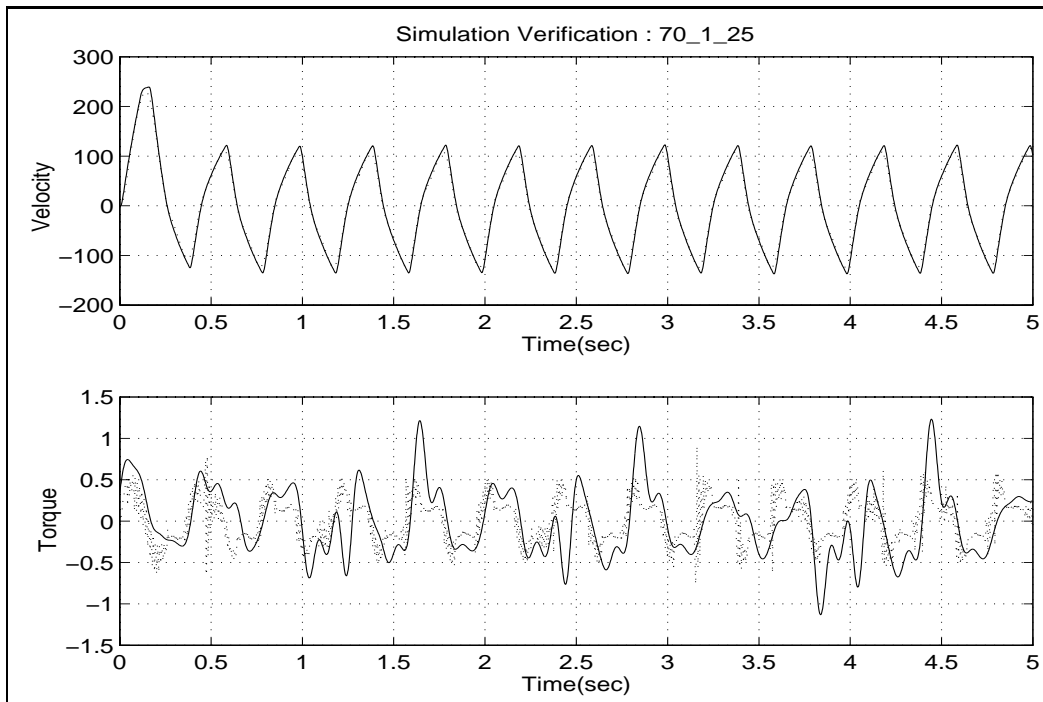


FIGURE 60. Free-motion simulation verification: 2.5 Hz sinusoid input

CENTER FOR INTELLIGENT MACHINES, MCGILL UNIVERSITY, 3480 UNIVERSITY ST., MONTRÉAL  
(QUÉBEC) H3A 2A7, CANADA, *Tel.* : (514) 398-8202  
*E-mail address:* taghirad@cim.mcgill.ca